Random Errors in the Stable Boundary Layer: Implications for Modern Observational Techniques

BRIAN R. GREENE[a,b] AND SCOTT T. SALESKY[a]

[a] *School of Meteorology, University of Oklahoma, Norman, Oklahoma*
[b] *Cooperative Institute for Severe and High-Impact Weather Research and Operations, University of Oklahoma, Norman, Oklahoma*

(Manuscript received 16 May 2022, in final form 17 October 2022)

ABSTRACT: For decades, stable boundary layer (SBL) turbulence has proven challenging to measure, parameterize, simulate, and interpret. Uncrewed aircraft systems (UAS) are becoming a reliable method to sample the atmospheric boundary layer, offering new perspectives for understanding the SBL. Moreover, continual computational advances have enabled the use of large-eddy simulations (LES) to simulate the atmosphere at ever-smaller scales. LES is therefore a powerful tool in establishing a baseline framework to understand the extent to which vertical profiles from UAS can represent larger-scale SBL flows. To quantify the representativeness of observations from UAS profiles and eddy-covariance observations within the SBL, we performed a random error analysis using a suite of six large-eddy simulations for a wide range of stabilities. We combine these random error estimates with emulated observations of a UAS and eddy-covariance systems to better inform future observational studies. For each experiment, we estimate relative random errors using the so-called relaxed filtering method for first- and second-order moments as functions of height and averaging time. We show that the random errors can be on the same order of magnitude as other instrument-based errors due to bias or dynamic response. Unlike instrument errors, however, random errors decrease with averaging time. For these reasons, we recommend coupling UAS observations with other ground-based instruments as well as dynamically adjusting the UAS vertical ascent rate to account for how errors change with height and stability.

SIGNIFICANCE STATEMENT: Weather-sensing uncrewed aircraft systems are rapidly being realized as effective tools to collect valuable observations within the atmospheric boundary layer. To fully capitalize on this novel observational technique, it is necessary to develop an understanding of how well their observations can represent the surrounding atmosphere across various spatial and temporal scales. In this study we quantify the representativeness of atmospheric observations in the stable boundary layer by evaluating the random errors for parameters such as temperature, wind speed, and fluxes as estimated from a suite of large-eddy simulations. Our results can better inform future studies utilizing uncrewed aircraft systems by highlighting how random errors in their observations relate to vertical ascent rate, atmospheric stability, and measurement height.

KEYWORDS: Turbulence; Boundary layer; Stability; Error analysis; Uncertainty; Large eddy simulations

1. Introduction

Although dynamics within the stable atmospheric boundary layer (SBL) have far-reaching implications from pollution dispersion to wind energy production, it is also notoriously difficult to collect representative turbulence measurements within the SBL. This is because turbulent motions are often orders of magnitude smaller than flow processes controlling mean quantities, and small-scale processes can easily be obscured by mesoscale features. Numerical weather prediction (NWP) models commonly struggle to forecast winds and temperature near the surface, which is due in part to a fundamental lack of knowledge of how to represent turbulence within the SBL (Steeneveld et al. 2008; Sandu et al. 2013; Holtslag et al. 2013). Fortunately, recent advances in observational techniques are enabling previously unattainable investigations into these processes.

Measurements using uncrewed aircraft systems (UASs; Joyce et al. 2021) are showing promise in bridging the so-called data gap in the atmospheric boundary layer (ABL; e.g., Chilson et al. 2019; Pinto et al. 2021; Houston et al. 2021, and references therein). In particular, UASs are capable of measuring the same atmospheric parameters as traditional radiosondes with comparable accuracy (Bell et al. 2020) while also offering significantly improved vertical resolution, mobility, and experimental control. Several recent field campaigns have also incorporated UASs, such as the Innovative Strategies for Observations in the Arctic Atmospheric Boundary Layer campaign (ISOBAR; Kral et al. 2018, 2021; Greene et al. 2022) and the Lower Atmospheric Profiling Studies at Elevation–A Remotely Piloted Aircraft Team Experiment (LAPSE-RATE; de Boer et al. 2020a,b). The UASs featured in these campaigns fall into one of two main categories: rotary- and fixed-wing. Rotary-wing UASs include both commercial off-the-shelf aircraft outfitted with sensors (e.g., Islam et al. 2021) as well as custom-built multicopters such as the University of Oklahoma Copter-Sonde (Segales et al. 2020; Pillar-Little et al. 2021). These rotary-wing UASs are typically best suited for collecting observations in vertical profiles, where they offer high vertical and temporal resolution for analysis of vertical gradients (e.g.,

Corresponding author: Brian R. Greene, brian.greene@ou.edu

DOI: 10.1175/JAS-D-22-0096.1

Lappin et al. 2022; Greene et al. 2022). In contrast, fixed-wing UASs are capable of carrying heavier payloads with longer flight endurances as compared to rotary-wing UASs. Fixed-wing UASs are therefore better suited for carrying sensor packages containing turbulence-resolving instruments (e.g., Wildmann et al. 2014; Rautenberg et al. 2019; Alaoui-Sosse et al. 2022; de Boer et al. 2022) or bulky chemical species and aerosol instruments (e.g., Schuyler and Guzman 2017; Krautwurst et al. 2021).

Some potential avenues for understanding the ability of UAS observations to improve NWP models include case studies with novel data assimilation techniques (Flagg et al. 2018; Jensen et al. 2021, 2022) as well as observing system simulation experiments (OSSEs; Moore 2018; Chilson et al. 2019; Shenoy 2021). These techniques all require characterization of the uncertainties involved with the UAS observations, which for simplicity are typically assumed to be constant and related to general sensor biases. Considerable progress has been made in recent years to characterize uncertainties in UAS observations due to sensor placement (Greene et al. 2018, 2019; Barbieri et al. 2019), sensor response times (Houston and Keeler 2018, 2020; Segales et al. 2022), and improved wind vector estimations (González-Rocha et al. 2019, 2020). Although these studies have been critical for establishing UAS technology as a legitimate observational technique, few studies have examined how well these novel platforms can characterize atmospheric flow at larger scales.

A relatively unexplored method of assessing the representativeness of observations within the SBL is through an analysis of random errors, which arise due to averaging a stochastic signal over an insufficient time period for the time mean to converge to the true ensemble mean by the ergodic hypothesis (Lumley and Panofsky 1964; Sreenivasan et al. 1978; Mann and Lenschow 1994; Lenschow et al. 1994). Random errors fundamentally differ from those due to instrument bias, imprecision, or dynamic response, as random errors are mitigated by increased averaging time whereas instrumental errors are relatively unaffected by this and instead require regular calibration. For context, random errors can still be on the same order of magnitude as instrumental errors for many parameters (Salesky et al. 2012; Salesky and Chamecki 2012; Bell et al. 2020), and theoretically all these errors independently compound. In this study, we leverage a suite of large-eddy simulations (LES) to estimate the random errors for various first- and second-order turbulence moments at typical averaging periods along with emulated observations by UAS and eddy-covariance systems within the SBL to answer the following key questions:

1) How do random errors depend on atmospheric stability and measurement height for various first- and second-order turbulence moments?
2) How well do emulated UAS and eddy-covariance measurements represent the ensemble mean?
3) What considerations are necessary to mitigate random errors for observations in the SBL?

This study is organized as follows: We provide the background theory for and methods to estimate random errors in stochastic signals in section 2. In section 3 we describe our LES code as well as the parameter space of simulations conducted. We then provide an overview for how we adapted existing methods for random error estimation for use with volumetric LES output in section 4 and present results in section 5. A discussion on the significance of these results is presented in section 6 before a summary and concluding remarks in section 7.

2. Random errors and the relaxed filtering method

As discussed previously, random errors emerge when a time series is not averaged long enough for the time mean to converge sufficiently to the true ensemble mean via the ergodic hypothesis (Lumley and Panofsky 1964; Sreenivasan et al. 1978; Mann and Lenschow 1994; Lenschow et al. 1994). For a given random variable f, we are therefore interested in the ability of its temporal mean $\overline{f}$ to approximate the ensemble mean $\langle f \rangle$. Herein we define temporal averaging with an overbar $\overline{(\cdot)}$ and ensemble averaging with brackets $\langle \cdot \rangle$. Lumley and Panofsky (1964) describe the random error of f in terms of its error variance $\sigma^2_{\overline{f}}$ over an averaging period T:

$$\sigma^2_{\overline{f}}(T) = \left\langle \left[\frac{1}{T} \int_{t_0 - T/2}^{t_0 + T/2} f(t) dt - \langle f \rangle \right]^2 \right\rangle = \langle [\overline{f} - \langle f \rangle]^2 \rangle. \tag{1}$$

They further show that by assuming statistical stationarity, the error variance of f can be related to its integral time scale $\mathcal{T}_f$ as

$$\sigma^2_{\overline{f}}(T) = \frac{\langle f'^2 \rangle}{N} = \frac{2\mathcal{T}_f \langle f'^2 \rangle}{T}, \tag{2}$$

where $\langle f'^2 \rangle = \langle [f - \langle f \rangle]^2 \rangle$ is the ensemble variance of f and $N = T/(2\mathcal{T}_f)$ is the number of independent samples. It is then possible to define a relative error by normalizing the error standard deviation by the ensemble mean, $\epsilon_f = \sigma_{\overline{f}}/|\langle f \rangle|$, which yields

$$\epsilon_f = \left[\frac{2\mathcal{T}_f \langle f'^2 \rangle}{\langle f \rangle^2 T} \right]^{1/2}. \tag{3}$$

A major drawback of using Eq. (3) to calculate relative random errors stems from the difficulty in computing the integral time scale $\mathcal{T}_f$ (if it exists at all; see discussion in Dias et al. 2004). In general, the integral time scale of f can be defined as

$$\mathcal{T}_f = \int_0^\infty \rho(\tau) d\tau, \tag{4}$$

where $\rho(\tau)$ is the autocorrelation function of f as a function of lag τ, which is defined as

$$\rho(\tau) = \frac{\langle [f(t) - \langle f \rangle][f(t + \tau) - \langle f \rangle] \rangle}{\langle f'^2 \rangle}. \tag{5}$$

To use Eq. (4) for computing the integral time scale for any real signal, one must impose an upper bound of integration. This upper bound may be arbitrarily large, but common choices include the first zero crossing of $\rho(\tau)$ (e.g., Sreenivasan et al. 1978; Lenschow et al. 1994; Salesky et al. 2012), when

$\rho(\tau) = e^{-1}$, or at the minimum point of the autocorrelation (Tritton 1988; Theunissen et al. 2008). Moreover, it is possible to assume an exponential form of the autocorrelation function (Lenschow et al. 1994; Kaimal and Finnigan 1994; Sullivan et al. 2003) or fit a lag-window function (Dias et al. 2004) in order to compute the integral. Ultimately, the computed value of $\mathcal{T}_f$ is highly sensitive to the choice of integration method, which may not necessarily converge implying the nonexistence of the integral time scale. In addition to these computational difficulties, a physical constraint on accurately calculating an integral time scale depends heavily on the assumption of stationarity in the time series itself. A nonstationary process may possess an autocorrelation function that does not converge toward zero, which would result in an unbounded integral scale. Statistical preprocessing techniques such as linear detrending may mitigate the effects of nonstationarity in windows of ≈1 h, but is not always guaranteed.

It is therefore apparent that one's ability to determine relative random errors is impeded by the difficulty in accurately calculating integral time and length scales. To circumvent these difficulties, Finkelstein and Sims (2001) introduced a statistical method for calculating the variance of a covariance that is based on a sample's auto and cross covariance functions. While shown to be effective for observational time series data across a wide range of environments, this method is only suited for estimating the relative random errors in second-order turbulence moments. Additionally, Salesky et al. (2012) proposed the so-called filtering method, which uses a spatially local flux decomposition to recover a power-law fit for the error variance of any parameter as a function of averaging time (or averaging length in the case of spatial filters). The premise is based on the commutative nature of linear filters, which requires that the vertical flux $\overline{w'c'}$ of some quantity c averaged over length L is equivalent to an average of separately filtered fluxes $\widetilde{w'c'}$ (Sagaut 2006; Salesky et al. 2012). Using this commutative property, the standard deviation of the local flux $\widetilde{w'c'}$, $\sigma_{\widetilde{w'c'}}$, can be related to the filter width Δ via a power law of the form

$$\sigma_{\widetilde{w'c'}}(\Delta) = C_{wc}\Delta^{-1/2}, \tag{6}$$

where the coefficient C_{wc} is determined via least squares. The relative random error of the flux for any given averaging length L can therefore be determined without a priori knowledge of the integral length scale by evaluating Eq. (6) at $\Delta = L$ and normalizing by the mean flux as

$$\epsilon_{wc} = \frac{\sigma_{\widetilde{w'c'}}(L)}{\langle w'c' \rangle}. \tag{7}$$

If desired, it is then possible to recover the integral scale a posteriori through a combination of Eqs. (6) and (2).

Dias et al. (2018) later expanded upon the work by Salesky et al. (2012) by acknowledging that fixing the −1/2 exponent in Eq. (6) still implies the existence of an integral length scale. They argued that for a wide variety of real-world applications, Hurst's phenomenon of long-term persistence (Hurst 1951; O'Connell et al. 2016) will cause this exponent to deviate from −1/2 and that a more general approach may be more appropriate. By letting this exponent vary freely, Dias et al. (2018) proposed a relaxed filtering method (RFM) that is capable of determining error statistics even when an integral scale does not exist. The RFM thus relies on a generalized form of Eq. (6), which takes the form

$$\sigma_{\widetilde{w'c'}}(\Delta) = C_{wc}\Delta^{-p/2}, \tag{8}$$

where the exponent p is allowed to vary freely and can be determined through least squares regression. In this framework, Dias et al. (2018) showed analytically that $0 < p < 1$ is evidence for Hurst's phenomenon in a stochastic process. Dias et al. (2018) also noted that the errors estimated by the RFM generally are higher than those from the method of Lumley and Panofsky (1964) in Eq. (3) due to accounting for the presence of Hurst's phenomenon. Moreover, as Eq. (3) directly requires that the exponent $p = 1$ in Eq. (8), error estimates from the RFM may not necessarily enable one to calculate an integral length scale a posteriori as in Salesky et al. (2012). Readers are directed to the works of Salesky et al. (2012) and Dias et al. (2018) for the mathematical justification for this technique. Although we present the general premise for the RFM in terms of second-order turbulent moments in Eqs. (6)–(8), this technique is valid in estimating relative random errors in turbulence moments of any order including, for example, the mean velocity or potential temperature. We further expand upon the implementation of the RFM using LES volumetric output in section 4.

3. Large-eddy simulations

a. Code description

We utilize LES code based on Albertson and Parlange (1999) and Kumar et al. (2006), which solves the filtered rotational form of the incompressible Navier–Stokes equations for momentum and potential temperature, respectively:

$$\frac{\partial \tilde{u}_i}{\partial t} + \tilde{u}_j\left(\frac{\partial \tilde{u}_i}{\partial x_j} - \frac{\partial \tilde{u}_j}{\partial x_i}\right) = -\frac{1}{\rho}\frac{\partial \tilde{p}^*}{\partial x_i} + g\left(\frac{\tilde{\theta} - \langle\tilde{\theta}\rangle_{xy}}{\langle\tilde{\theta}\rangle_{xy}}\right)\delta_{i3} - \frac{\partial \tau_{ij}}{\partial x_j} + f(\tilde{u}_2 - V_g)\delta_{i1} - f(\tilde{u}_1 - U_g)\delta_{i2}, \tag{9}$$

$$\frac{\partial \tilde{\theta}}{\partial t} + \tilde{u}_j\frac{\partial \tilde{\theta}}{\partial x_j} = -\frac{\partial \pi_j^\theta}{\partial x_j}. \tag{10}$$

In this context, the tilde denotes a filtered quantity, $\tilde{u}_i$ denotes the filtered velocity vector with $i = 1, 2, 3$ representing streamwise, spanwise, and wall-normal components (respectively), $\tilde{p}^* = \tilde{p} + (1/2)\rho\tilde{u}_i^2$ is the modified pressure, θ is potential temperature, δ_{ij} is the Kronecker delta, $\tau_{ij} = \widetilde{u_i u_j} - \tilde{u}_i\tilde{u}_j$ is the SGS stress tensor, $\pi_j^\theta = \widetilde{\theta u_j} - \tilde{\theta}\tilde{u}_j$ is the SGS potential temperature flux, (U_g, V_g) are the geostrophic wind components, and $g = 9.81$ m s^{-2} is the acceleration due to gravity. Brackets with the subscript xy denote horizontal planar averaging. Spatial derivatives are calculated pseudospectrally in

TABLE 1. Mean simulation properties for cases A–F averaged over the last physical hour of the simulation, including the surface cooling rate C_r, SBL height h, surface friction velocity u_{*0}, surface potential temperature scale θ_{*0}, Obukhov length L, global stability h/L, ratio of LLJ to SBL depth z_j/h, bulk SBL inversion strength $\Delta\langle\theta\rangle/\Delta z$, eddy turnover period T_L, and number of large-eddy turnover times nT_L.

Case	C_r (K h^{-1})	h (m)	u_{*0} (m s^{-1})	θ_{*0} (K)	L (m)	h/L (—)	z_j/h (—)	$\Delta\langle\theta\rangle/\Delta z$ (K km^{-1})	$T_L = h/u_{*0}$ (s)	nT_L (—)
A	0.25	160	0.231	0.0383	93.5	1.71	0.976	10.2	692	5.2
B	0.5	135	0.211	0.0658	45.1	3.00	0.935	24.1	642	5.6
C	1.0	107	0.190	0.112	21.1	5.07	0.911	59.7	563	6.4
D	1.5	93.7	0.180	0.157	13.3	7.05	0.928	101	521	6.9
E	2.0	87.1	0.172	0.198	9.51	9.16	0.926	147	506	7.1
F	2.5	80.5	0.166	0.236	7.28	11.1	0.924	198	485	7.4

the horizontal plane and via second-order centered finite differencing in the vertical, and the second-order Adams–Bashforth method is utilized for time integration. The subgrid-scale (SGS) model is based on the Lagrangian-averaged scale-dependent model described by Bou-Zeid et al. (2005), and the wall model is based on Monin–Obukhov similarity theory (MOST; Monin and Obukhov 1954) applied locally with test filtering at a scale twice the grid spacing to improve average stress profiles (Bou-Zeid et al. 2005). For simulating the SBL, we prescribe a surface temperature with a constant cooling rate as the lower boundary condition. The upper boundary condition is stress-free and impenetrable, and a sponge layer is applied in the upper 25% of the domain after Nieuwstadt et al. (1993). The LES code is parallelized in horizontal (xy) slabs using message passing interface (MPI; Aoyama and Nakano 1999).

b. Cases

To simulate the SBL with LES, we impose a lower boundary condition as a prescribed constant cooling rate $C_r = -\partial\langle\theta_0\rangle/\partial t$ at the surface coupled with a wall model to determine surface heat fluxes (e.g., Basu et al. 2008; Gibbs et al. 2015). Here we simulate a series of six idealized SBL cases A–F after those by Huang and Bou-Zeid (2013), which were in turn based on those by Kosović and Curry (2000) (Table 1). Kosović and Curry (2000) originally utilized constant surface cooling rates based on observations from the Beaufort Sea Arctic Stratus Experiment and has been the inspiration for numerous other SBL studies using LES (e.g., Beare et al. 2006; Sullivan et al. 2016; Maronga et al. 2020; Stoll et al. 2020, and references therein). The six cases presented by Huang and Bou-Zeid (2013) vary only in their prescribed values of C_r, and as such were easily adapted for our purposes.

Our simulated domain was fixed at $(L_x, L_y, L_z) = (800, 800, 400)$ m with a horizontally homogeneous land surface of aerodynamic roughness length $z_0 = 0.1$ m. The domain size is sufficiently large relative to the integral length scales ($L_x \approx 10\mathcal{L}$) so that our results are not expected to be influenced significantly by the periodic boundary conditions employed in the horizontal directions. In our code, the roughness lengths for momentum and heat, z_{0m} and z_{0h}, are chosen to be equal for consistency with previous studies. We imposed a constant geostrophic wind of $U_g = 8$ m s^{-1} along with a Coriolis parameter of $f = 1.318 \times 10^{-4}$ s^{-1} corresponding to a latitude of 65°N. The initial temperature profile (including the surface) was set to a constant 265 K up to a height of $z = 100$ m, above which the temperature increased with a constant inversion strength $\partial\theta/\partial z = 0.01$ K m^{-1}.

Due to computational expense, we initialize and run each simulated case on a domain with $n = n_x \times n_y \times n_z = 96^3$ total grid points for six hours of physical time before interpolating to a grid with $n = 192^3$ grid points and simulating for four more hours. At the higher resolution, this equates to a grid spacing of $\Delta_f = (\Delta_x\Delta_y\Delta_z)^{1/3} = 3.31$ m. This resolution was selected after performing grid convergence tests with $n \in \{96^3, 128^3, 160^3, 192^3\}$ (see appendix). Our time step Δ_t was set to a constant 0.04 s during the spinup simulations, which was then decreased to a value of 0.02 s in each of the interpolated cases for numerical stability. Ensemble means are calculated by averaging in horizontal planes and in time over the last hour of simulation (i.e., $\langle\cdot\rangle = \langle\cdot\rangle_{xyt}$), which corresponds to 5.4–7.7 large-eddy turnover times ($T_L = h/u_{*0}$, Table 1) and is consistent with other idealized investigations of the SBL (e.g., Huang and Bou-Zeid 2013; Sullivan et al. 2016; van der Linden et al. 2019; Maronga and Li 2021). Additional analysis of time series output of numerous simulated parameters as well as SBL depth and Obukhov length indicate this final hour is quasi stationary (not shown). To further improve statistical convergence when calculating second-order turbulent parameters, all first-order fields are linearly detrended in time.

Bulk properties from the six simulations are summarized in Table 1. We determine the SBL height h after the mean stress profile technique by Beare et al. (2006): h is the height where the mean stress u_*^2 first falls to less than 5% of its surface value of u_{*0}^2 and divided by 0.95. With this definition we ensure the majority of turbulent motions are contained within the SBL. In this framework,

$$u_*^2 = (\langle u'w'\rangle^2 + \langle v'w'\rangle^2)^{1/2} \tag{11}$$

represents the magnitude of the vertical kinematic momentum flux, and the subscript 0 denotes the value of a quantity at the lowest grid level. The Obukhov length $L = u_{*0}^2\langle\theta_0\rangle/\kappa g\theta_{*0}$ depends on the von Kármán constant $\kappa = 0.4$, and the potential temperature scale $\theta_* = -\langle\theta'w'\rangle/u_*$. The height of the low-level jet (LLJ) is denoted as z_j, and we estimate a bulk SBL inversion strength using the top and bottom grid points within the SBL: $\Delta\langle\theta\rangle/\Delta z = (\langle\theta(z = h)\rangle - \langle\theta(z = \Delta_z/2)\rangle)/(h - \Delta_z/2)$.

For each of these cases, we consider both mean profiles as well as emulated observations from UAS and eddy-covariance

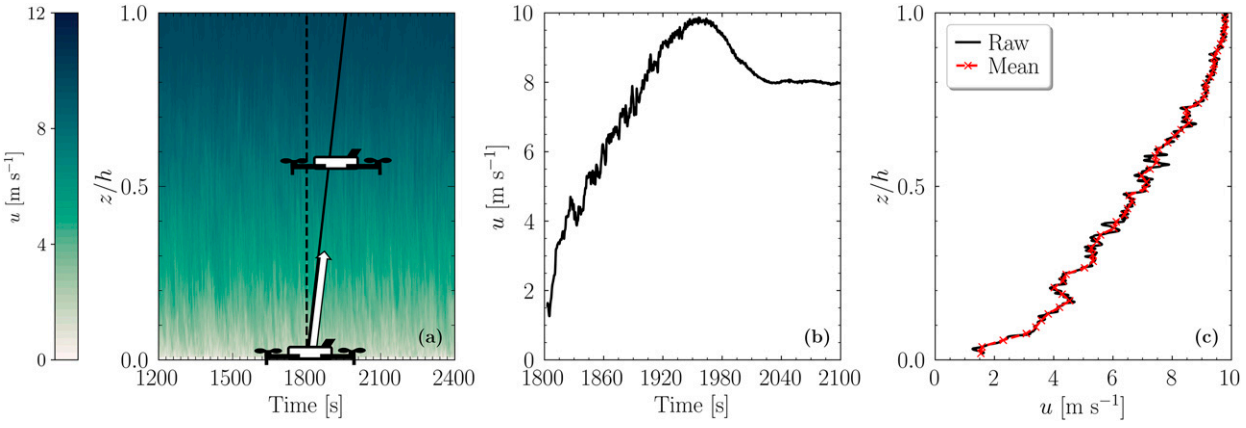

FIG. 1. (a) Emulated trajectory of a rotary-wing UAS ascending at a constant rate of 1 m s^{-1} (solid line) and an instantaneous trajectory (dashed line) overlaid upon a time–height cross section of u from a virtual tower in the center of the LES domain, (b) time series of u velocity sampled by the virtual UAS, and (c) resulting vertical profile of wind speed in its raw state (black) and averaged into 3 m vertical bins (red).

vertical profiles. The emulated UAS and eddy-covariance profiles are derived from a virtual tower similar to that described by Salesky and Anderson (2018): it is located at $(x, y) = (L_x/2, L_y/2)$ and outputs a time series of each of the simulated parameters at every gridpoint in the vertical and at every simulated time step (recall that $\Delta_t = 0.02$ s), yielding data with dimensions of height and time (Fig. 1a). By assuming a constant UAS ascent rate, we can determine a time series of its corresponding vertical coordinates, which we then match and subsample from interpolated virtual tower data (Fig. 1b). We then average the resulting one-dimensional time series in the same way as is customary for true UAS data (e.g., Pillar-Little et al. 2021; Greene et al. 2022) to obtain an emulated UAS profile with a constant vertical resolution (Fig. 1c).

In this analysis we utilize averaging times of 3 s and 30 min for first- and second-order moments, respectively. These times were chosen with regard to typical averaging time scales when operating a UAS (3 s) or eddy-covariance system (30 min). Within the SBL it is common for a rotary-wing UAS to ascend at approximately 1 m s^{-1} and to postprocess the data into altitude bins 3 m high, which corresponds to an averaging time of about 3 s (e.g., Greene et al. 2022). In general, UAS data are processed with emphasis on the resulting vertical resolution instead of the averaging time for each vertical bin. Vertical ascent rates from UAS are also typically chosen to optimize the aircraft's ability to reach a targeted maximum height with regards for sensor response times. It is also common practice to average over blocks varying from 10 to 60 min when calculating turbulence moments from mast-mounted eddy-covariance systems. Thus, we chose the 30-min averaging time as representative of a typical application.

4. Relaxed filtering method applied to large-eddy simulation output

In this section we describe how we adapted the relaxed filtering method algorithm from time series output analyzed in Salesky et al. (2012) and Dias et al. (2018) for use with volumetric data generated by LES. We implement the RFM for a given variable $f = f(x, y, z, t)$ by first calculating its error variance through the following steps:

1) Isolate a "pencil" slice of f along the streamwise (x) dimension at a constant value of y, z, t (Fig. 2a, black curve).
2) Apply an idealized top-hat filter spatially with filter width Δ (Fig. 2a, colored curves).
3) Calculate the variance of the filtered signal, $\sigma_{\tilde{f}}^2$.
4) Repeat steps 2 and 3 using 50 different filter widths spaced logarithmically such that $\Delta \in [\Delta_x, L_x]$ to attain $\sigma_{\tilde{f}}^2(\Delta)$.
5) Repeat steps 1–4 for all y, z, and t in the final physical hour of simulation.
6) Average the variances in y and t to finally obtain a two-dimensional error variance that is a function of both filter width and height: $\sigma_{\tilde{f}}^2 = \sigma_{\tilde{f}}^2(\Delta, z)$.

An example of steps 1–6 is presented in Fig. 2a for $f = u$, which includes the resulting spatial distributions after 4 levels of filtering. Calculating error variance along x followed by averaging in y and t method can be interpreted as averaging a row of instrumented towers spanning the y direction individually measuring the streamwise flow. Variations on this technique (e.g., filtering in both x and y and averaging only in t) are beyond the scope of this study, but the horizontal homogeneity of the simulations would likely lead to similar conclusions as this study.

After calculating the error variance for a given parameter, the remaining procedure to estimate its corresponding relative random error for a desired sampling time closely resembles that from Salesky et al. (2012):

7) For a given z, normalize the error variance by its corresponding ensemble variance $\langle f'^2 \rangle$ (Fig. 2b, solid curve).
8) Select a range of filter widths to isolate the normalized error variance (Fig. 2b, $\Delta^{\min}$ and $\Delta^{\max}$).
9) Fit a function of the form $\sigma_{\tilde{f}}^2/\langle f'^2 \rangle = C_f \Delta^{-p}$ [similar to Eq. (8) except utilizing the error variance instead of

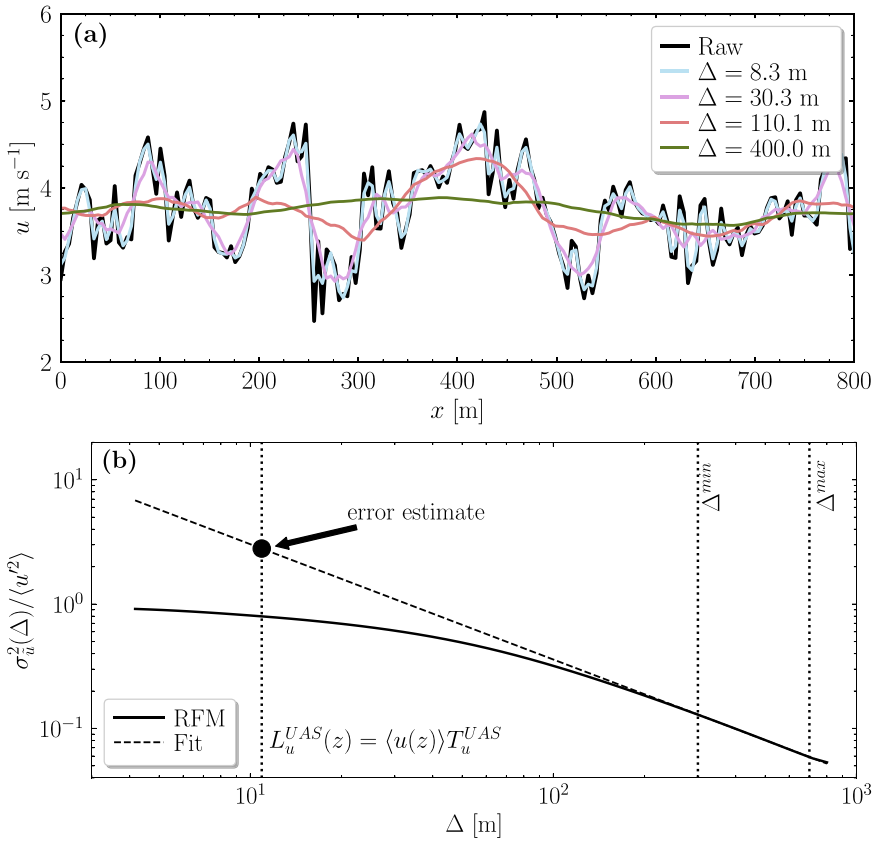

FIG. 2. Graphic demonstration of the relaxed filtering method applied to volumetric LES data. (a) Raw u vs streamwise distance x from case A centered spanwise in the domain and at a height of $z/h = 0.14$ (black) overlaid with iterations of the signal filtered at varying scales Δ. (b) y- and time-averaged variances of u as a function of filter scale Δ (RFM, solid curve) to which Eq. (8) is fit between $\Delta^{\min}$ and $\Delta^{\max}$ (Fit, dashed line); adapted from Fig. 2 in Salesky et al. (2012). An error estimate for a UAS sampling time scale T_u^{UAS} can then be extracted from the power law.

standard deviation] within the window selected in step 8 (Fig. 2b, dashed line).

10) Estimate the relative random error of f for a desired sampling time T by converting to a length L through Taylor's hypothesis and substituting into the empirical power law for normalized error variance obtained in the previous step (Fig. 2b, black dot).
11) Repeat steps 7–10 for all heights to obtain $\sigma_{\bar{f}}^2(L,z)/\langle f'^2(z)\rangle$.
12) Finally, compute the relative random error $\epsilon_{\bar{f}}(L,z) = \sigma_{\bar{f}}(L,z)/\langle f(z)\rangle$ using the corresponding ensemble mean.

Note that in step 8 we choose the window of 300–700 m to fit the power law, which corresponds closely to the $\mathcal{O}(10\text{–}100)$ s denoted by Salesky et al. (2012) when invoking Taylor's hypothesis. This power law is theoretically valid for extrapolation to any scale Δ, as seen in Fig. 2b for a UAS sampling scale L_u^{UAS} that happens to be within the range $[\Delta_x, L_x]$ where the error variance has also explicitly been calculated. In this particular case, it is still advantageous in an applied sense to utilize the extrapolated power law over what would effectively be a lookup table with the understanding that random error estimates by the RFM are larger than those by other direct methods (Dias et al. 2018).

The decision to perform the RFM in spatial coordinates instead of in the time dimension also warrants a brief discussion. With considerations for hard disk drive storage space, it is not computationally feasible to save every single volumetric output for the total of 1.26×10^6 time steps. At our prescribed output frequency, the resulting temporal resolution would equate to an order of magnitude worse spatial resolution when invoking Taylor's hypothesis, so to retain as much information as possible we iterate over individual streamwise segments as described previously. In the case that we did perform the RFM in temporal coordinates, then step 10 would no longer be necessary as one could simply input the desired sampling time directly into the derived power law.

To determine errors in wind speed $u_h = (\langle u\rangle^2 + \langle v\rangle^2)^{1/2}$, wind direction $\alpha = \arctan(\langle u\rangle/\langle v\rangle)$, and momentum flux u_*^2, we implement error propagation based on these parameters' functional dependence on the direct LES output of u, v, $\langle u'w'\rangle$, and $\langle v'w'\rangle$. In general, for a given variable c with functional dependence on the variables a, b [i.e., $c = f(a, b)$], it is possible to relate all of their error variances based on a Taylor

expansion (e.g., Bevington and Robinson 1969; Salesky and Chamecki 2012) as

$$\sigma_c^2 \approx \sigma_a^2\left(\frac{\partial c}{\partial a}\right)^2 + \sigma_b^2\left(\frac{\partial c}{\partial b}\right)^2 + 2\,\mathrm{Cov}(a,b)\frac{\partial c}{\partial a}\,\frac{\partial c}{\partial b}, \tag{12}$$

where $\mathrm{Cov}(a, b)$ is the covariance between the errors in a and b. In practice, this third error covariance term on the right-hand side of Eq. (12) is difficult to calculate or interpret even with full volumetric output from LES. We assume that all errors are uncorrelated, thereby neglecting this term in further calculations. Applying Eq. (12) to estimate relative random errors in u_h, α, and u_*^2 gives us the following expressions:

$$\epsilon_{u_h} = \frac{\sigma_{u_h}}{|\langle u_h\rangle|} \approx \frac{1}{\langle u_h\rangle}\left(\frac{\sigma_{u^\dagger}^2\langle u^\dagger\rangle^2 + \sigma_{v^\dagger}^2\langle v^\dagger\rangle^2}{\langle u^\dagger\rangle^2 + \langle v^\dagger\rangle^2}\right)^{1/2}, \tag{13a}$$

$$\epsilon_{\alpha} = \frac{\sigma_{\alpha}}{|\langle \alpha\rangle|} \approx \frac{1}{\langle \alpha\rangle}\left[\frac{\sigma_{u^\dagger}^2\langle v^\dagger\rangle^2 + \sigma_{v^\dagger}^2\langle u^\dagger\rangle^2}{(\langle u^\dagger\rangle^2 + \langle v^\dagger\rangle^2)^2}\right]^{1/2}, \tag{13b}$$

and

$$\epsilon_{u_*^2} = \frac{\sigma_{u_*^2}}{|u_*^2|} \approx \frac{1}{u_*^2}\left(\frac{\sigma_{u'w'}^2\langle u'w'\rangle^2 + \sigma_{v'w'}^2\langle v'w'\rangle^2}{u_*^4}\right)^{1/2}. \tag{13c}$$

Note that when performing the error propagation calculations using Eq. (13), we use the unrotated forms of u and v, denoted $u^\dagger$ and $v^\dagger$, along with their associated errors from the RFM.

5. Results

In this section we provide a general overview with the simulated mean profiles for each of cases A–F in section 5a, consider the stability and height dependence of random errors in section 5c, and consider implications of random errors to observations collected by UAS and eddy covariance in sections 5d and 5e, respectively.

a. Mean profiles and instantaneous fields

In general, the wind speed profiles (Fig. 3a) do not change drastically with stability, although there are subtle differences in curvature for $z/h < 0.4$. The low-level jet height z_j relative to the SBL height h is also largely unaffected by stability (see Table 1). The wind direction profiles (Fig. 3b) are also relatively insensitive to stability, and one can see a general veering with height consistent with the canonical idealized SBL (e.g., Zilitinkevich 1989). The potential temperature profiles (Fig. 3c) demonstrate mean lapse rates that increase strongly with surface cooling rates, as expected (Table 1).

The profiles of nondimensional momentum and heat fluxes (Figs. 3d,e) collapse to common curves, with irregularities in the lowest few grid points likely induced by the wall model. These profiles compare well with the results from Huang and Bou-Zeid (2013) for their cases A–F. We acknowledge the collapse of these profiles in particular is sensitive to the choice in defining the SBL height h. For example, Sullivan et al. (2016) define their SBL height based on the mean potential temperature gradient. Regardless, this general collapse indicates the quasi stationarity for these second-order moments as required for an appropriate random error analysis.

Both the gradient and flux Richardson numbers (Ri_g and Ri_f, respectively) increase strongly with height and stability (Fig. 3f). Here we define Ri_g and Ri_f as

$$\mathrm{Ri}_g = \frac{g}{\langle\theta\rangle_0}\,\frac{\partial\langle\theta\rangle}{\partial z}\left[\left(\frac{\partial\langle u^\dagger\rangle}{\partial z}\right)^2 + \left(\frac{\partial\langle v^\dagger\rangle}{\partial z}\right)^2\right]^{-1}, \tag{14a}$$

$$\mathrm{Ri}_f = \frac{g\langle\theta' w'\rangle}{\langle\theta\rangle_0}\left[\langle u'w'\rangle\,\frac{\partial\langle u^\dagger\rangle}{\partial z} + \langle v'w'\rangle\frac{\partial\langle v^\dagger\rangle}{\partial z}\right]^{-1}. \tag{14b}$$

This results in a turbulent Prandtl number $\mathrm{Pr}_t = \mathrm{Ri}_g/\mathrm{Ri}_f$ profile that is relatively constant with height with values between 0.6 and 0.7 (not shown).

The nondimensional streamwise and vertical velocity variances (Figs. 3g,h) display similar trends where the variances generally decrease with stability in the middle of the SBL. Enhanced levels of $\langle u'^2\rangle$ between $0.2 < z/h < 0.6$ for cases E and F could be signatures of intermittent turbulence or related to inertial oscillations within the SBL. Finally, the nondimensional potential temperature variance (Fig. 3i) follows two general trends dependent on stability. In cases A and B the variance generally increases from the surface up to $z/h \approx 0.2$, remains constant up to $z/h \approx 0.6$, and then decreases with height. Variances in cases C–F peak close to the surface and generally decrease with height monotonically for $z/h > 0.2$. Common across all cases, however, is that for $z/h < 0.1$, variance generally increases with stability. The implications for this pattern will be discussed further in section 5c.

For a qualitative comparison between cases A and F, Fig. 4 portrays instantaneous x–z cross sections in the center of the domain for scaled streamwise velocity and potential temperature. In case A (Figs. 4a,b) there is evidence of turbulent motions with pockets of high and low momentum throughout as well as quasi-organized structures within the temperature fields (e.g., between $1.0 < x/h < 1.8$ and $0.3 < z/h < 0.75$) reminiscent of the microfronts observed by Sullivan et al. (2016). Case F (Figs. 4c,d) appears far more quiescent, as one may expect for strongly stable conditions. Both the velocity and temperature fields are highly stratified, and the vertical extent of eddies are considerably smaller than those in case A. This perspective supports the expectation that in general, we would expect integral length scales in the SBL to decrease with increasing stability.

b. Integral length scales

To provide context for the random error profiles in the following section, in Fig. 5 we include the integral length scales of first-order parameters determined from the volumetric LES output. These length scales were calculated along individual streamwise samples of the full volumetric field by integrating the sample's spatial autocorrelation function until the first zero crossing. This process was repeated and averaged over all y and time steps as in the RFM described in section 4, resulting in vertical profiles of integral length scales, $\mathcal{L}(z)$.

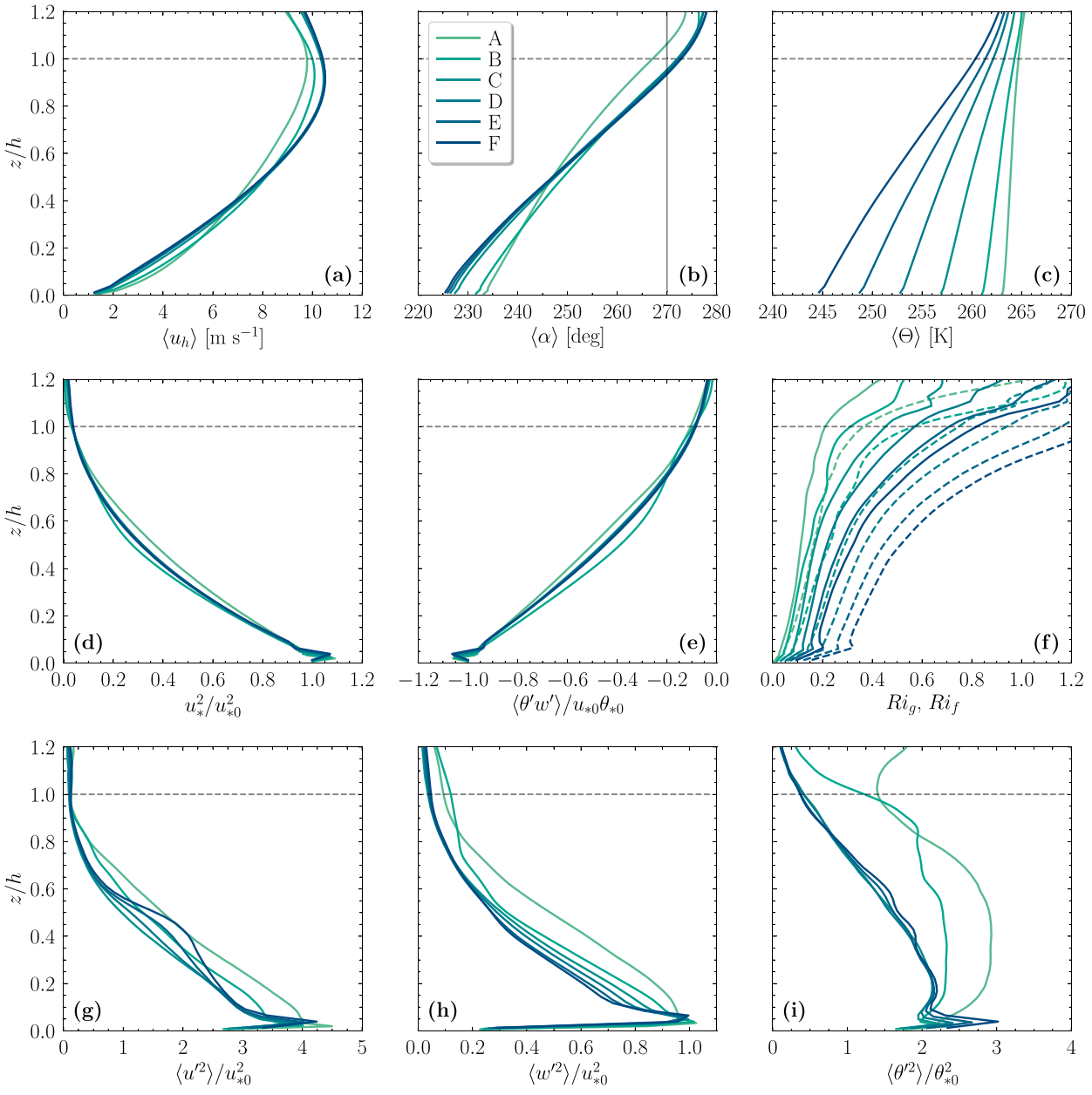

FIG. 3. Mean profiles of (a) wind speed, (b) wind direction, (c) potential temperature, (d) total (resolved plus SGS) momentum flux, (e) total heat flux, (f) bulk Richardson number (solid) and flux Richardson number (dashed), (g) streamwise velocity variance, (h) vertical velocity variance, and (i) potential temperature variance for all cases A–F as a function of z/h. For (d)–(i), quantities are scaled by surface values of u_* and θ_* where appropriate.

For all parameters it is readily apparent that the integral scales decrease at all heights with stability. For weak stability, there is a peak in $\mathcal{L}_u$ around $0.5 < z/h < 0.7$, just below the level of the LLJ (Fig. 3a), whereas with increasing stability these scales remain generally constant with height for $0.2 < z/h < 0.8$ (Fig. 5a). In general, $\mathcal{L}_u$ is larger than $\mathcal{L}_w$ for all stabilities and heights (Fig. 5b), and is comparable in magnitude to $\mathcal{L}_\theta$ (Fig. 5c). For cases C–F, $\mathcal{L}_w$ is of similar length to the LES filter scale Δ_f below the LLJ, indicating that buoyancy strongly acts to suppress vertical turbulent mixing through the characteristic size of eddies.

The integral scale profiles for cases A–C are generally on par with those presented by Huang and Bou-Zeid (2013) (note that they did not include an estimate for the potential temperature length scale), most notably in the shape of the peaks in $\mathcal{L}_u$ and the strong increase in $\mathcal{L}_w$ with height for $z/h > 0.6$. Interestingly, for cases D–F, our results do not indicate the strong peak in $\mathcal{L}_u$ around $z/h \approx 0.4$ that they reported

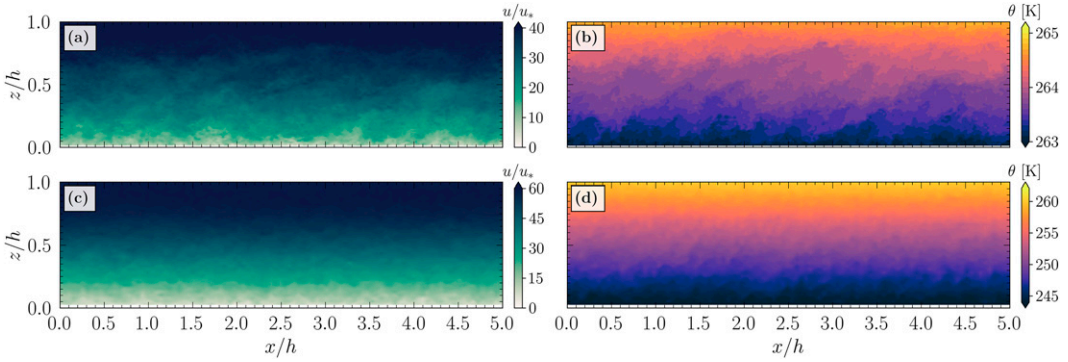

FIG. 4. Instantaneous x–z cross sections at $y = L_y/2$ of (left) scaled streamwise velocity and (right) potential temperature for simulations (top) A and (bottom) F.

being related to buoyantly flattened coherent structures. Although our simulations are based on those by Huang and Bou-Zeid (2013) and other mean profiles compare strongly (Fig. 3) to theirs, determining the reasoning behind these discrepancies in integral scales is outside the scope of this study.

c. *Random error profiles*

Utilizing the RFM outlined in sections 2 and 4, in Fig. 6 we show relative random errors for the first-order thermodynamic and kinematic parameters typically observed with UASs as a function of stability and z/h. It is apparent that errors generally decrease with height and stability for wind speed and direction (Figs. 6a,b), which can logically follow from the premise that integral length scales for velocity components decrease with stability (Figs. 5a,b), and larger errors are associated with longer integral length scales via Eq. (2). This is additionally supported by the fact that the dimensional values of streamwise velocity variance also decreases with stability (Fig. 3g, recall from Table 1 that u_{*0} decreases with stability) which would necessitate longer averaging times at weak stability to constrain the natural variability in the flow. To the contrary, relative random errors in potential temperature actually increase with stability (Fig. 6c), and do not decrease as strongly with height. While possibly counterintuitive at first, this potential temperature error pattern can be justified physically as follows. As surface cooling increases with global stability, the near-surface lapse rates increase in magnitude more rapidly. From Lumley and Panofsky (1964) and Wyngaard and Cot (1971), this temporally evolving temperature gradient is a source term in potential temperature variance (given a stationary heat flux, which is generally valid in this case), which would correspondingly increase the amount of averaging time necessary for a time series mean to converge toward the ensemble mean potential temperature. This is also consistent with the mean profiles of potential temperature variance (Fig. 3i) wherein the dimensional value of $\langle \theta'^2 \rangle$ generally increases with stability (again recall from Table 1 that θ_{*0} increases by an order of magnitude between cases A and F and therefore so do the dimensional variances). Therefore, stronger stability begets larger ϵ_θ, as seen in Fig. 6c.

For all profiles, and especially at lower stabilities, the near-surface wind speed errors are substantial (i.e., >25%). For context, a relative random error of 25% implies that a wind speed of 2 m s^{-1} near the surface could result in an error standard deviation of at least 0.5 m s^{-1} due just to the limited averaging time. Additionally, a 0.1% error from an observed $\theta = 250$ K results in an absolute error of only 0.25 K. These errors are on the same order of magnitude as those due to calibration

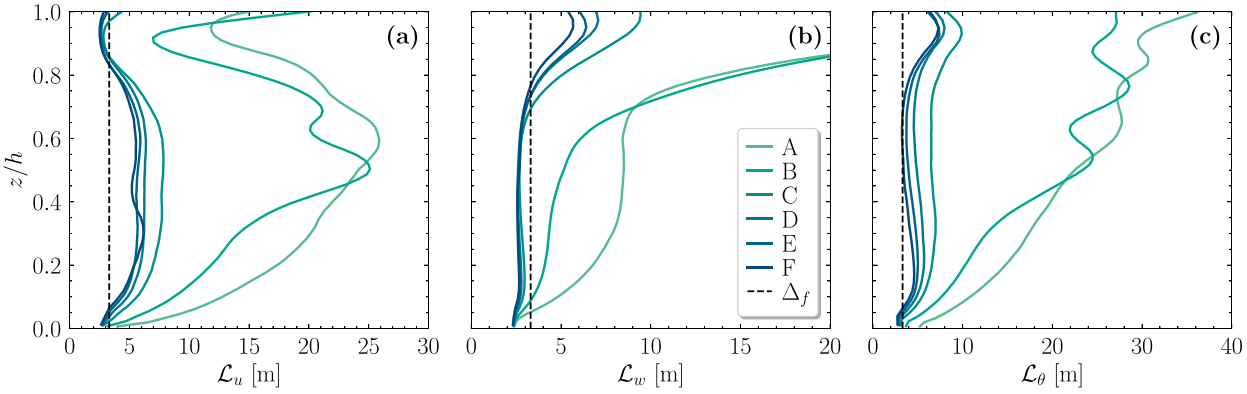

FIG. 5. Profiles of integral length scales for (a) streamwise velocity, (b) vertical velocity, and (c) potential temperature for all six cases A–F. The LES filter width Δ_f is plotted as a vertical dashed black line for reference.

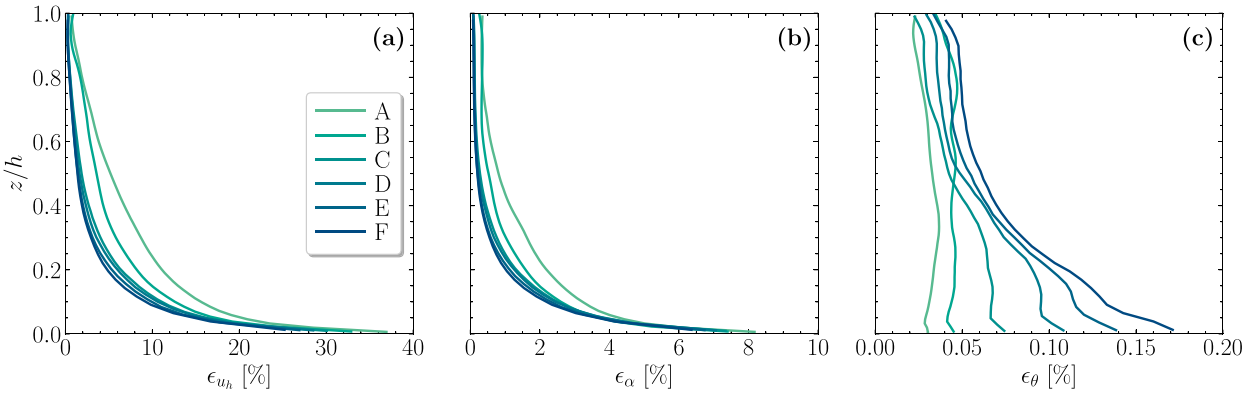

FIG. 6. Profiles of relative random errors for (a) wind speed, (b) wind direction, and (c) potential temperature for all six cases A–F. Errors are calculated based on 3 s averaging times consistent with typical UAS observation processing.

and instrument uncertainty, which are independent of each other and therefore are compounded. For example, the CopterSonde rotary-wing UAS is accurate to within 0.6 m s^{-1} and 0.5°C compared against radiosondes (Segales et al. 2020; Bell et al. 2020). The most direct solution to offset these errors is to increase the averaging times in the lower SBL, which is then a trade-off between UAS vertical ascent rates and the vertical resolution desired (discussed further in section 5d).

The relative random errors for second-order moments based on 30-min averaging times (Fig. 7) also generally decrease with stability. Recall that we utilize 30-min averaging times for these parameters, which is consistent with typical values used with the eddy-covariance method. The errors in Reynolds stresses are relatively constant between 5% and 15% from the surface up to $z/h \approx 0.7$ (Fig. 7a). Due to the way we define h as a linear extrapolation to where $u_*^2 \to 0$, and since u_*^2 appears in the denominator when calculating $\epsilon_{u_*^2}$ via Eq. (13c), the errors near the top of the SBL grow to be considerably larger than near the surface. To a lesser extent this pattern also occur near the top of the SBL for $\epsilon_{\overline{\theta' w'}}$ for cases A–C, likely for similar reasons (Fig. 7b).

The errors for heat flux across all cases (Fig. 7b) nearly double from the surface to $z/h \approx 0.07$ for all cases. This may be indicative of surface layer processes, although it could also be an artifact of the LES wall model. For $0.15 < z/h < 0.7$, $\epsilon_{\overline{\theta' w'}}$ appears to organize into two categories: increasing slowly with height (cases A and B) and decreasing slowly with height (cases C–F). These two groups likely correspond to differing regimes of fully turbulent flow in weakly stable stratification versus generally weak vertical mixing at higher stability.

The error profiles of velocity and potential temperature variances (Figs. 7c,d,e) also exhibit this clustering into two primary groups of 1) cases A and B, and 2) cases C–F. The $\epsilon_{\overline{u'u'}}$ and $\epsilon_{\overline{\theta' w'}}$ profiles peak around $z/h \approx 0.7$ for group 1, and group 2 does not necessarily peak but rather decreases continuously throughout the SBL. For all cases, however, the magnitudes of the relative errors are consistently in the 5%–20% range for streamwise velocity variance and even narrower ranges of 2%–8% for vertical velocity variance and 3%–12% for potential temperature variance. These results are consistent with the notion that turbulence intensity within increasingly stable regimes should become weaker, resulting in increasingly localized motions with smaller integral scales (as also hinted to by Fig. 5). The general decrease in height for the second-order errors combined with decreasing variability for higher stabilities is also consistent with the "z-less" scaling

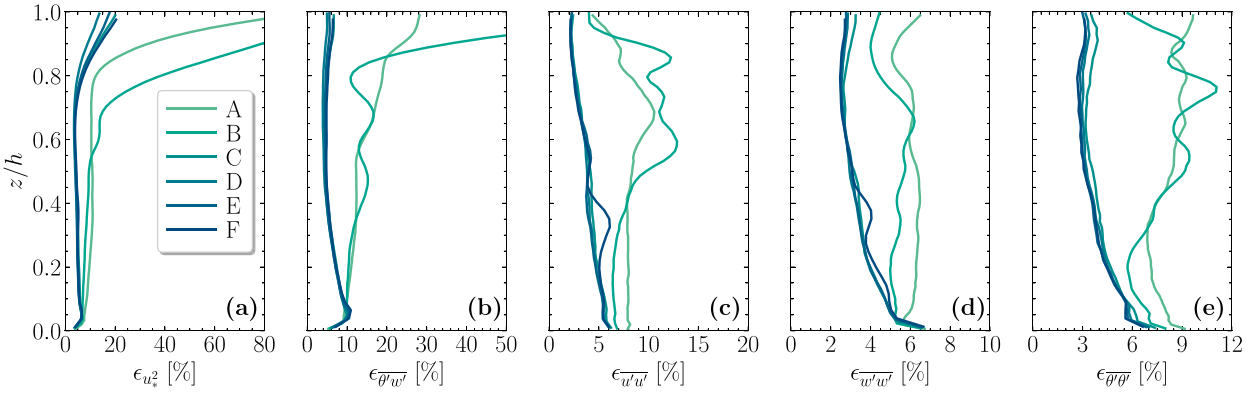

FIG. 7. Profiles of relative random errors for (a) momentum flux, (b) potential temperature flux, (c) streamwise velocity variance, (d) vertical velocity variance, and (e) potential temperature variance for all six cases A–F. Errors are calculated based on 30-min averaging times consistent with typical eddy-covariance measurements.

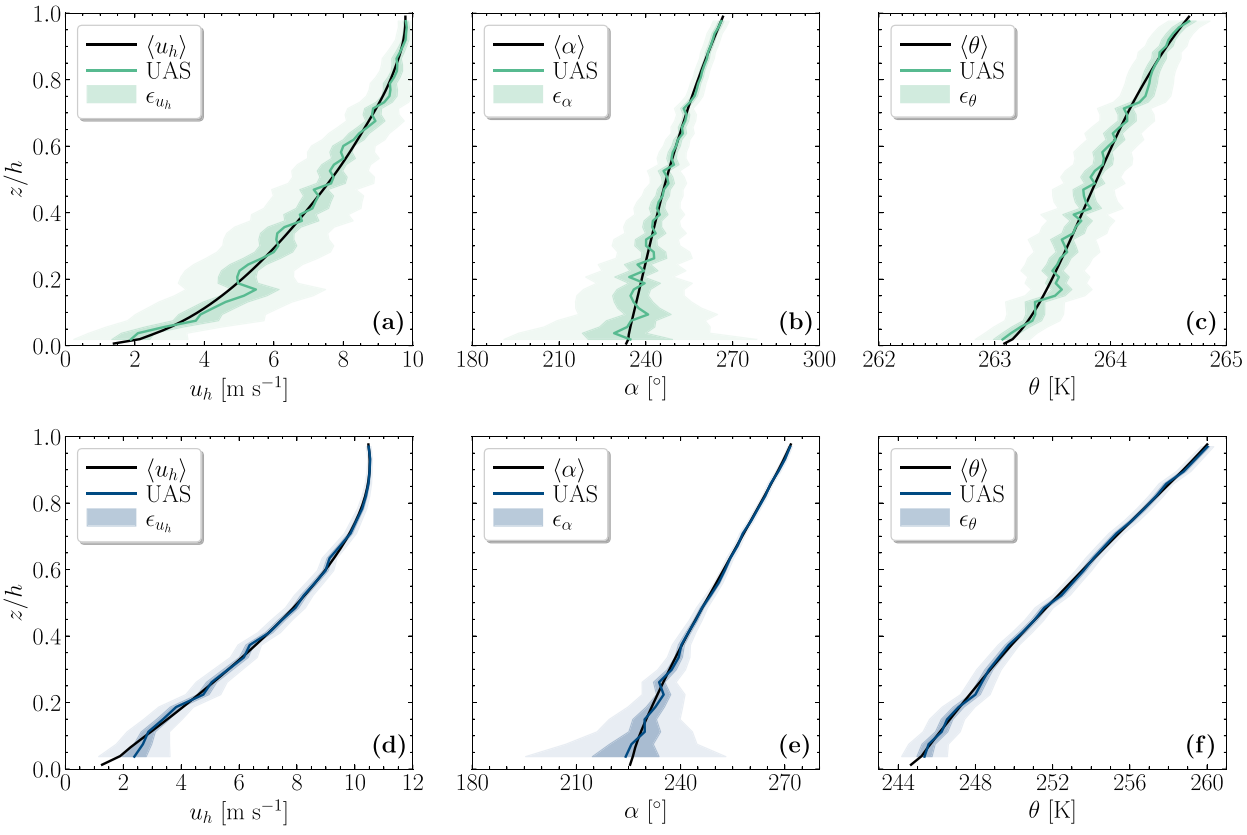

FIG. 8. Profiles of (left) wind speed, (center) wind direction, and (right) potential temperature from cases (top) A and (bottom) F. The solid black line in each is the horizontally and temporally averaged ensemble mean reproduced from Fig. 3. Each colored solid line represents observations from an emulated UAS profile ascending at 1 m s^{-1} and averaged in 3 s bins. Dark (light) shading denotes 1 (3) error standard deviations.

regime. This is because the distance from the ground loses relevance as a characteristic length for higher stratification as turbulence becomes more localized and mixing lengths depend more on parameters such as wind shear and buoyancy frequency (e.g., van de Wiel et al. 2008; Huang et al. 2013; Sorbjan 2017; Greene et al. 2022). Since these parameters do not change dramatically with height in the quasi-stationary cases presented, it is reasonable to conclude that the corresponding second-order integral length scales would similarly remain relatively constant with height, thereby resulting in the observed profiles of relative random errors in the second-order moments.

The exponent p determined by least squares fitting of Eq. (8) lies within the range $0.8 < p < 1.2$ for all parameters shown at all heights and stabilities (not shown). This corresponds to a similar range in the Hurst exponent H as found Dias et al. (2018) using sonic anemometer data, indicating that Hurst's phenomenon is indeed influencing the flow dynamics. Therefore, error estimates by the RFM will generally exceed those by the Lumley and Panofsky method of Eq. (1) and the existence of an integral scale is dubious (Dias et al. 2004, 2018). Regardless, we include these integral scales (Fig. 5) for improved physical understanding of the random error results.

d. *Implications for uncrewed aircraft system measurements*

A UAS takes a finite amount of time to fly a vertical profile, and the atmosphere is continually evolving while it does so. Figure 1 conceptualizes this for a UAS ascending at 1 m s^{-1} through the depth of the SBL, which in this case would take about three minutes to reach a height of $z = h$. In this section we emulate a rotary-wing UAS ascending through the simulated domain at a fixed rate as described in section 3b. Note that these emulated profiles assume idealized thermodynamic and kinematic sensors free from bias, imprecision, or dynamic response errors, as we are strictly interested in the impact of random errors on observed profiles. Finally, we calculate random error bounds for these emulated profiles based on the results from the previous section for comparison with the ensemble mean profiles (i.e., Fig. 3). These error bounds physically represent the error standard deviation σ_f for a given parameter f due to inadequate sampling time [recall Eqs. (1) and (8)], which we refer to succinctly as the random error. They are determined by combining an observed parameter $f_{\text{obs}}(z)$ with its corresponding relative random error $\epsilon_f(z)$ as $\sigma_f(z) = f_{\text{obs}}(z)\epsilon_f(z)$ to yield a dimensional value. In Fig. 8 (and later in Fig. 11), these dimensional values of random error are shaded around the emulated observation values at each

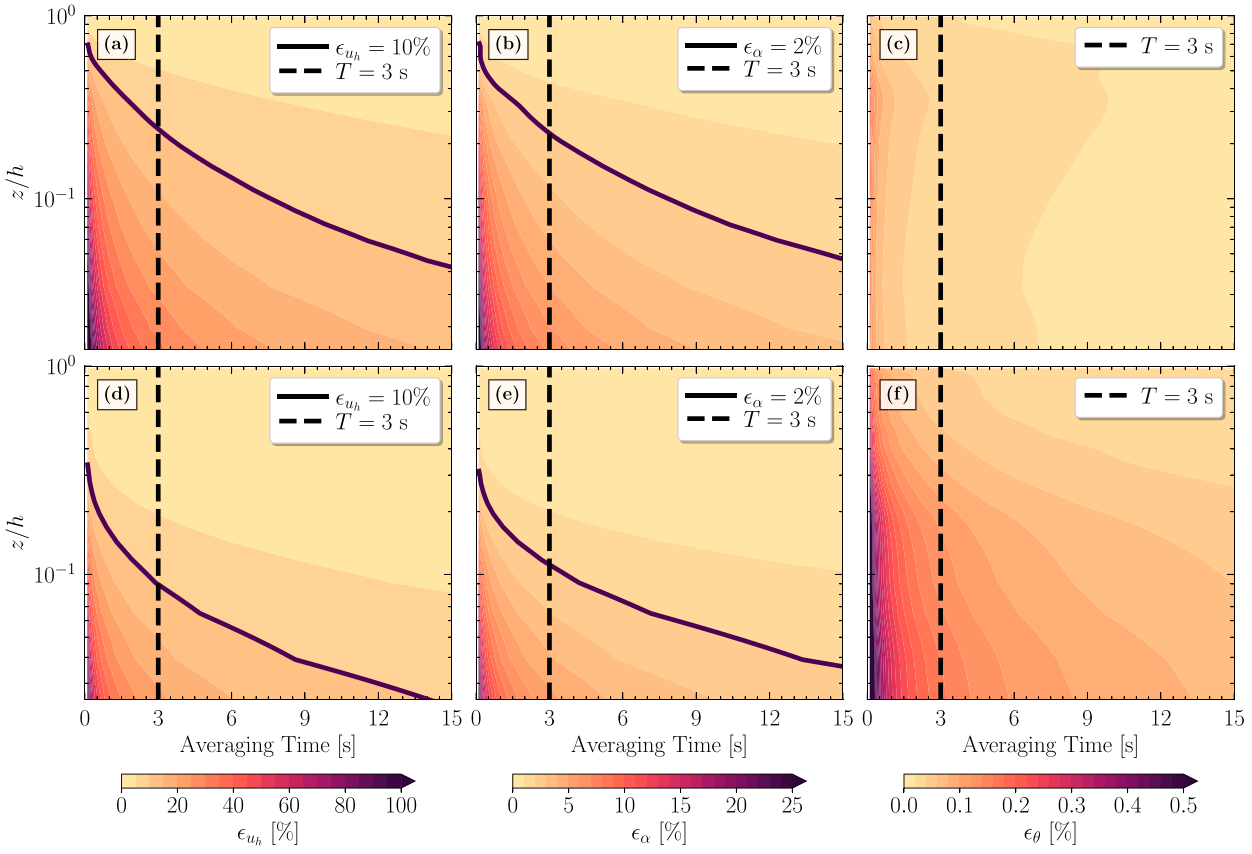

FIG. 9. Contours of relative random errors in (left) wind speed, (center) wind direction, and (right) potential temperature as functions of height and averaging time during cases (top) A and (bottom) F. For reference, the vertical dashed line denotes an averaging time of 3 s, and the solid black contours denote error levels of 10% in (a) and (d) and 2% in (b) and (e). Note that the y axis for each panel is logarithmic and the color scale range varies for each parameter.

height corresponding to the 1σ and 3σ levels, which should virtually capture the full range of random errors in an ensemble of realizations.

In Fig. 8 we demonstrate the ability of emulated UAS profiles to represent the ensemble mean for wind speed, wind direction, and potential temperature in cases A and F. In general, it is apparent that the UAS profiles are more variable with height in case A (Figs. 8a–c) as compared to case F (Figs. 8d–f). This is likely related to the integral length scales being smaller at high stability (Fig. 5) resulting in smaller random errors for case F. Each of these UAS profiles exhibit differences relative to their respective ensemble means, and these differences are also smaller for higher stability. For both cases A and F, the random errors in wind direction (Figs. 8b,e) near the surface are substantial at these averaging times, with 3σ ranges of around 90°. This is related to the relatively low wind speeds close to the surface, which some observational systems have difficulty measuring to begin with. We also note that the uncertainty range in wind speed for case A (Fig. 8a) spans between 0 and 4 m s^{-1} at the 3σ level, which may further add to operational difficulties in determining representative wind directions at weak stability. Although the emulated profiles of wind speed for case F (Fig. 8d) generally converge to the ensemble means on their own due to shorter integral length scales at high stabilities, it is still apparent that errors for $z/h < 0.2$ are on similar order of magnitude to the observations themselves.

With these results, it is therefore apparent that maintaining constant ascent rates (and corresponding constant averaging times) for UAS within the SBL may result in disproportionately large random errors close to the ground. To address this issue, Fig. 9 portrays the parameter space of relative errors contoured as functions of both z/h and averaging times for cases A and F. It is initially apparent that these errors drop off rapidly with averaging time, which follows directly from the power-law relationship fundamental to these estimations [Eq. (8)]. One can see that it is generally difficult to mitigate errors in u_h and α below $z/h < 0.1$ for both cases without averaging for an impractical amount of time, as UAS battery capacity becomes a limiting factor in the ability to sample the entire SBL in a single flight. This issue can potentially be overcome through pairing UAS operations with other continually sampling sensors such as eddy-covariance systems or ground-based remote sensors, which can be averaged arbitrarily long to supplement UAS profiles. It is additionally apparent from Figs. 9c and 9f that the errors in potential temperature are small (but not negligible) across the displayed

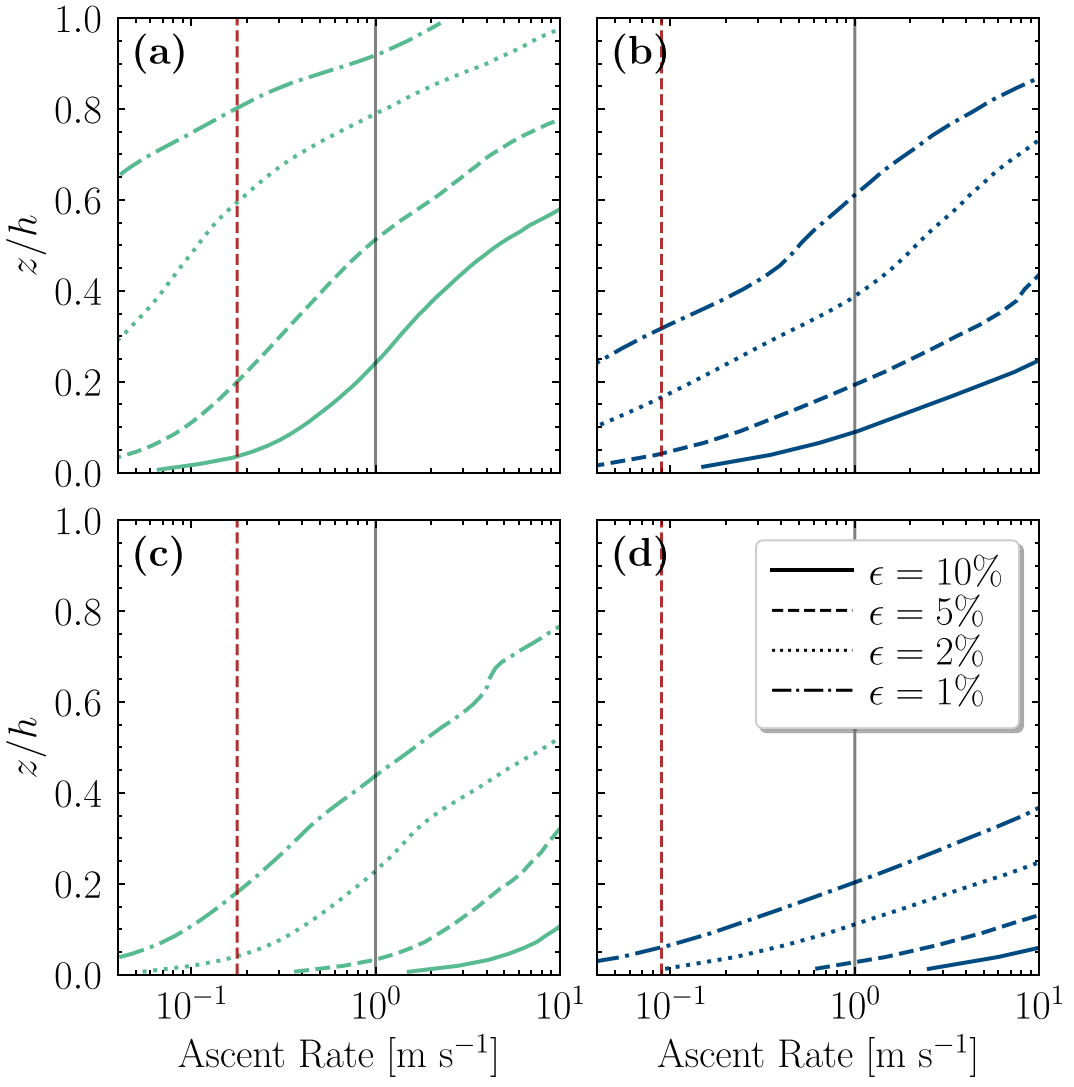

FIG. 10. Optimal ascent rates for various error levels for observations collected during an emulated UAS vertical profile with constant 3 m altitude bins for the following: (top) wind speed, (bottom) wind direction, (left) case A, (right) case F. For reference, a vertical solid gray line is included for a 1 m s^{-1} ascent rate, and the vertical dashed red lines denote the minimum constant ascent rate required to reach $z = h$ within 15 min.

parameter space. In case A there is little dependence on either z/h or averaging time, whereas these dependencies are modestly stronger in case F.

Due to the adaptive abilities of UAS technology, it is possible for a UAS operator to optimize a flight plan that accounts for random error dependencies on stability, height, and averaging time. For example, if an end user wishes to specify a threshold of random errors they deem acceptable, they would first need to obtain an estimate of atmospheric stability from, e.g., an instrumented tower to estimate the local surface cooling rate or Obukhov length, a ground-based remote sensor that can estimate the SBL depth, or the static stability as measured by a previous UAS flight or radiosonde launch to compare with the values in Table 1. It is also possible to estimate the dimensionless parameter z/L from multiple levels of tower-based observations utilizing Monin–Obukhov similarity functions (Launiainen and Vihma 1990). With this information, a UAS could be programmed in a predefined mission to ascend at variable rates. This variable ascent rate would enable a constant postprocessed vertical resolution and also takes into account the necessary amount of averaging time required at each height to reach the desired threshold. Figure 10 highlights this process for u_h and α in cases A and F assuming constant 3 m altitude bins after averaging. These bins were chosen as a trade-off between the accuracy of typical UAS autopilot altitude estimations and the desire to achieve the highest reasonable vertical resolution (see Greene et al. 2022). Note that we omitted the analysis ascent rate accounting for θ, as the averaging times necessary to approach $\epsilon = 1\%$ were so short that the ascent rate was effectively not a factor.

From Fig. 10 it is readily apparent that to achieve $\epsilon_{u_h} \leq 5\%$ for $z/h < 0.2$, a UAS must ascend with a vertical velocity v_z of $\mathcal{O}(0.01\text{–}0.1)\ \mathrm{m\ s^{-1}}$ across all stabilities. A similar trend is also discernible for ϵ_α, although relative random errors are generally smaller for α, and therefore, higher ascent rates are warranted. Herein lies a significant challenge when designing a UAS flight strategy: the total battery discharge time for a rotary-wing UAS utilizing lithium-polymer batteries such as the CopterSonde is generally ≈15 min (Segales et al. 2020). Ascending at $\leq 0.1\ \mathrm{m\ s^{-1}}$ for $z/h < 0.2$ would therefore not guarantee enough battery charge to ascend the full depth of the SBL. In Fig. 10 we visually represent this by overlaying the minimum ascent rate required to reach $z = h$ within 15 min. A UAS operator is thus presented with a trade-off when designing a flight strategy. They could either fly slowly close to the surface to minimize random errors but risk not sampling the entire SBL in one flight, or they could sacrifice the random error uncertainty to prioritize a maximum flight altitude.

In section 5e we continue this analysis for second-order moments that may be collected by eddy-covariance systems or fixed-wing UASs with a turbulence-resolving sensor payload.

e. *Implications for eddy-covariance measurements*

Determining second-order turbulence moments from observations within the SBL requires substantially longer averaging times than for first-order moments to achieve similar levels of relative random errors (see Fig. 7; Lenschow et al. 1994; Mann and Lenschow 1994; Dias et al. 2004). This concept will be especially important as sensors continue to miniaturize and both rotary- and fixed-wing UASs can more reliably collect turbulence-resolving observations. We again employ the virtual tower output described in section 3b to emulate eddy-covariance observations that are sampled simultaneously. This framework could be interpreted as 1) a tall instrumented tower or a collection of either 2) fixed-wing UASs flying at fixed-altitude circling within the horizontal domain or 3) vertically dispersed rotary-wing UASs hovering at a fixed position in space.

The resulting emulated profiles of normalized fluxes and variances are presented in Fig. 11 for cases A and F. One can see from Fig. 11 that in general the 30-min eddy-covariance profiles approximate the ensemble means reasonably well across the range of stabilities. The error bounds for each of the four second-order moments also encapsulate the ensemble mean profiles for virtually all heights and stabilities. The mean absolute differences between the emulated and ensemble mean profiles are also generally smaller for case F than case A, which follows the same trends we have observed throughout the study.

The emulated eddy-covariance profiles averaged over only 1 min depict a vastly different scenario. These 1-min profiles in case A vary substantially with height, with the only discernible trends being a gradual decrease with z/h (Figs. 11e–h). The case F 1-min profiles are at least on the same order of magnitude as the ensemble mean, but also demonstrate considerable variability with height (Figs. 11m–p). The corresponding random error bounds are also substantial, often on the same order of magnitude as the fluxes and variances themselves. While these results are perhaps unsurprising, they are provided as emphasis that many considerations are necessary to properly calculate physically meaningful second-order turbulence moments as it becomes more accessible to obtain the necessary observations with UAS.

To expand upon the two discrete averaging times for the emulated profiles demonstrated previously in Fig. 11, we consider the parameter space of averaging times as a function of stability, z/h, and desired level of relative random errors. In Fig. 12, one can draw the comparison to the framework presented in Fig. 10, except in this case we are concerned only with averaging times at each height. In case A (Figs. 12a–e) for example, it is difficult to achieve errors less than 5% near the surface, as the necessary averaging times exceed 1 h, and the ABL cannot always be expected to be quasi stationary over these long averaging periods. One is again potentially faced with a trade-off in the application of these results, and may need to compromise on the level of acceptable random errors for observations collected near the surface. On the contrary, achieving even a 10% error level is far more accessible across all stabilities, heights, and parameters, with averaging times ranging between 10 and 30 min. The velocity variance component error profiles in both cases (Figs. 12c,d,h,i) as well as potential temperature variance (Figs. 12e,j) require even shorter averaging times for $\epsilon > 10\%$ at all heights, at 15 min or less. These relatively short averaging times for the velocity variances are again indicative of the weak nature of turbulence intensity in the SBL that correspond to small integral length scales. For weak stability it generally requires more averaging time to constrain $\overline{u'u'}$ and $\overline{\theta'\theta'}$ than it does for $\overline{w'w'}$ for a given error level, but they become more comparable at high stability.

6. Discussion

Clearly there is no universal means to mitigate random errors for any of the considered first- and second-order turbulence moments. Even with careful experimental considerations for atmospheric stability, instrumentation heights, and averaging times, without access to an infinitely dense observational network, random errors are unavoidable for observations of real-world geophysical flows. We therefore analyze these results by contextualizing the random errors one might expect for their observations across a realistic parameter space.

Given the magnitude of errors in first-order moments near the surface, it may be difficult for a UAS to adequately sample for long enough and still reach the target maximum altitude on a single battery charge. For this reason, we recommend conducting UAS operations in proximity to surface-based observational systems whenever possible. Tower-mounted instruments and ground-based remote sensors (i.e., Doppler wind lidars, microwave radiometers, etc.) have the advantage of continually observing at a fixed location in space (Smith et al. 2019, 2021; Bonin et al. 2020). Therefore, the raw time series output from these sensors can be averaged at longer temporal periods than for UAS observations to mitigate random errors close to the surface.

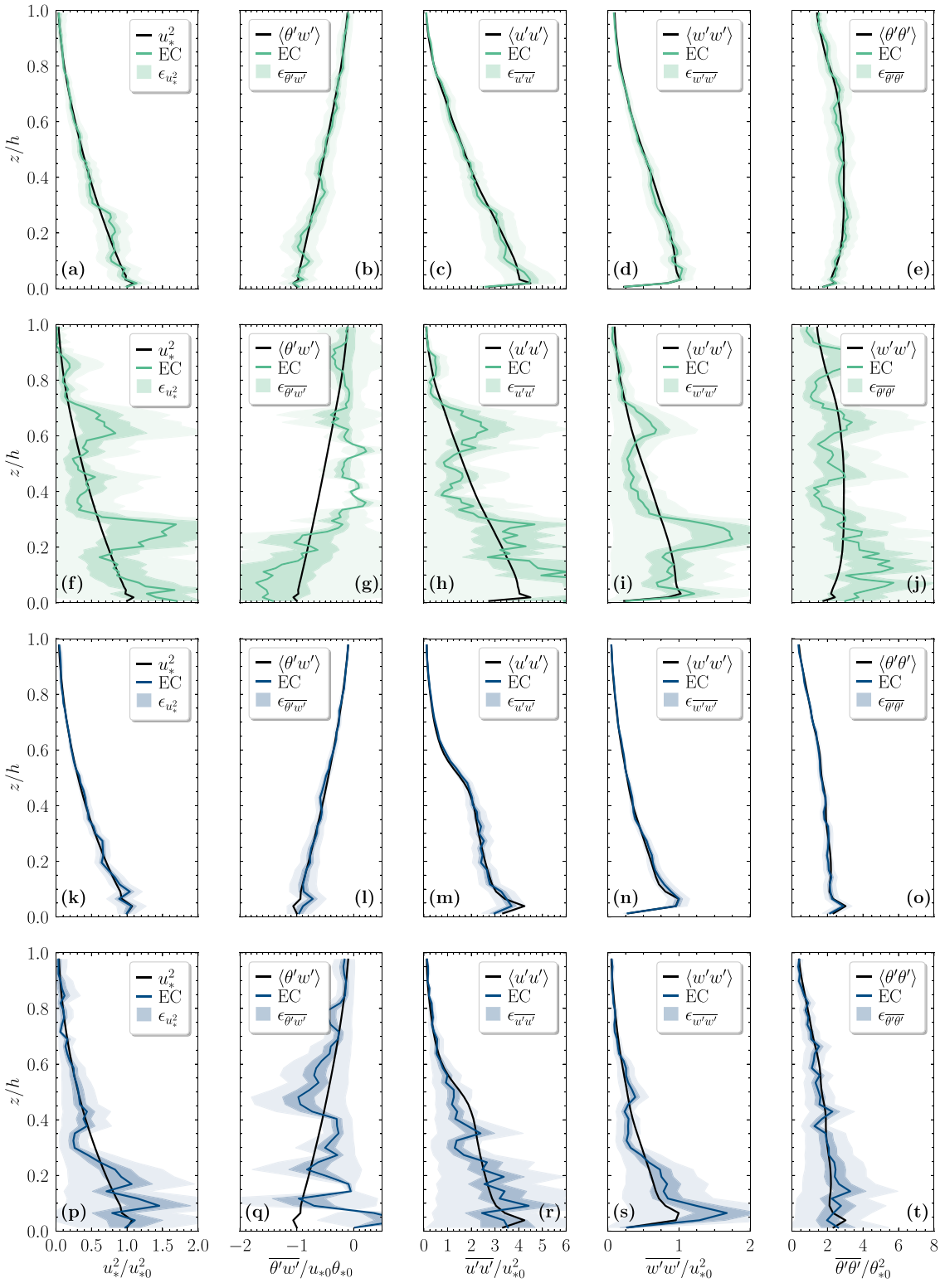

FIG. 11. Profiles of normalized (a),(f),(k),(p) momentum flux, (b),(g),(l),(q) heat flux, (c),(h),(m),(r) streamwise velocity variance, (d),(i),(n),(s) vertical velocity variance, and (e),(j),(o),(t) potential temperature variance from cases (row 1),(row 2) A and (row 3),(row 4) F. The emulated profiles are evaluated for 30 min averaging time in rows 1 and 3 and 1 min in rows 2 and 4. As in Fig. 8, the solid black lines denote the *xyt*-averaged LES output whereas the colored lines are emulated virtual eddy-covariance (EC) towers in the center of the domain. Dark (light) shading denotes 1 (3) standard deviation of random errors.

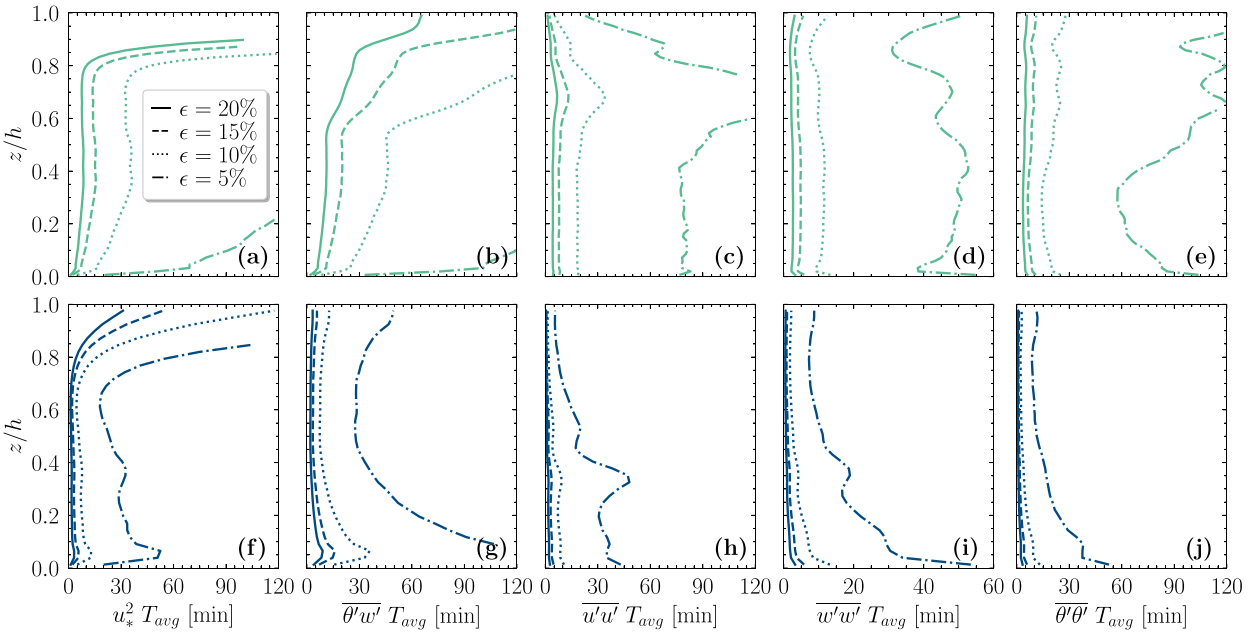

FIG. 12. Profiles of necessary eddy-covariance averaging times (T_{avg}) to reach specified levels of relative random error for cases (top) A and (bottom) F. The second-order moments include (a),(f) momentum flux, (b),(g) temperature flux, (c),(h) streamwise velocity variance, (d),(i) vertical velocity variance, and (e),(j) potential temperature variance.

Another possibility for improving the representativeness of UAS observations involves the temporal averaging of multiple vertical profiles as in Greene et al. (2022). This technique consists of averaging discontinuous subsamples of the overall atmospheric flow at a fixed point, which may have nonlinear impacts on the overall reduction in random errors. Similarly, one could also consider the averaging of multiple simultaneous UAS profiles distributed spatially within a target domain (Balsley et al. 2018; van den Heever et al. 2021). The exact quantification of these methods is beyond the scope of this study, but it logically follows that these would be effective methods of reducing random errors in general.

The quantification of random errors for potential temperature variance are of particular interest with regards to recent studies in the SBL using distributed temperature sensors compared with instrumented towers (Peltola et al. 2021), UAS (Higgins et al. 2018), and tethered balloons (Fritz et al. 2021; Lapo et al. 2022). As technology advances and rotary-wing UAS sensors continue to miniaturize, it is possible that potential temperature variance may be easier to observe directly when compared with velocity component variances, which typically rely on complex autopilot-based physical retrievals for estimates.

We acknowledge that this study only addresses an idealized parameter space with respect to the SBL. True geophysical flows are rarely characterized by horizontally homogeneous topography or land surface usage, and the diurnal cycle can drastically impact the assumption of stationarity. Regardless, the results from this study retain significant utility as a baseline of random errors, especially since the RFM has also been shown to produce larger estimates than through alternative methods (Dias et al. 2018).

It is important to note that random errors are not directly comparable with instrumental errors due to their underlying sources. Random errors are resultant of fundamental stochastic processes, and are to be interpreted as how well a given observation can represent the overall flow in an ensemble sense. This is not necessarily the same interpretation of instrumental biases or imprecision, which relate the ability of a sensor to describe its ambient environment at any given time. Further studies are necessary to determine how to best combine these sources of error for the purposes of NWP data assimilation of SBL observations.

Finally, as with any study with wall-modeled LES, reasonable uncertainty exists for all results close to the surface. This is largely due to the inability of LES to explicitly resolve turbulent motions in the viscous sublayer and instead relying on a wall model (in our case based on the dimensionless Monin–Obukhov similarity functions). Especially at higher stabilities, this may affect the resulting random error profiles close to the surface, although to what extent remains unknown. A recent pair of studies by Chinita et al. (2022a,b) used LES with a very small domain size and a 10 cm grid resolution to better resolve the surface layer of SBLs, which could potentially be suitable for comparisons with ground-based instrumented meteorological masts. A direct numerical simulation or wall-resolved LES would likewise provide more detailed information close to the wall, but these investigations are beyond the scope of the present study.

7. Conclusions

As UAS and eddy-covariance observations continue to demonstrate their utility for studies of the SBL, it is becoming

TABLE A1. Mean simulation properties for cases A and F for grid convergence. Here we include the x and z filter widths Δ_x and Δ_z, characteristic filter width $\Delta_f = (\Delta_x\Delta_y\Delta_x)^{1/3}$, time step Δ_t, and other parameters as in Table 1.

Case	Resolution (—)	Δ_x (m)	Δ_z (m)	Δ_f (m)	Δ_t (s)	h (m)	L (m)	h/L (—)	u_{*0} (m s^{-1})	z_i/h (—)
A	96^3	8.33	4.17	6.61	0.04	175	93.0	1.88	0.239	0.926
	128^3	6.25	3.12	4.96	0.02	167	91.2	1.84	0.232	0.950
	160^3	5.00	2.50	3.97	0.02	166	93.0	1.78	0.233	0.950
	192^3	4.17	2.08	3.31	0.02	160	93.5	1.71	0.231	0.976
F	96^3	8.33	4.17	6.61	0.04	99.7	7.64	13.1	0.177	0.908
	128^3	6.25	3.12	4.96	0.02	91.2	7.61	12.0	0.174	0.915
	160^3	5.00	2.50	3.97	0.02	83.4	7.47	11.2	0.170	0.950
	192^3	4.17	2.08	3.31	0.02	80.5	7.28	11.1	0.166	0.924

increasingly important to characterize how well these systems can represent the stably stratified flows at larger scales. In this study we address this issue through the lens of random error analyses of first- and second-order turbulence moments as estimated with the relaxed filtering method (Dias et al. 2018) applied to LES output. Our main findings from this study in the context of the scientific questions posed are as follows:

1) Random errors decrease with height for all first-order moments. Errors decrease with stability for wind speed and direction, but increase for potential temperature. In general, the errors in second-order moments are smaller than those in wind speed and potential temperature, but are strongly dependent on stability.
2) The emulated UAS and eddy-covariance profiles approximate the ensemble mean reasonably well for the cases shown, and the addition of the random error bounds explicitly demonstrates the representativeness of these profiles. Moreover, the emulated eddy-covariance profiles highlight the importance of sufficient averaging periods toward producing physically meaningful statistics.
3) Dynamically modifying the ascent rate of a UAS flying a vertical profile can be one method of decreasing the

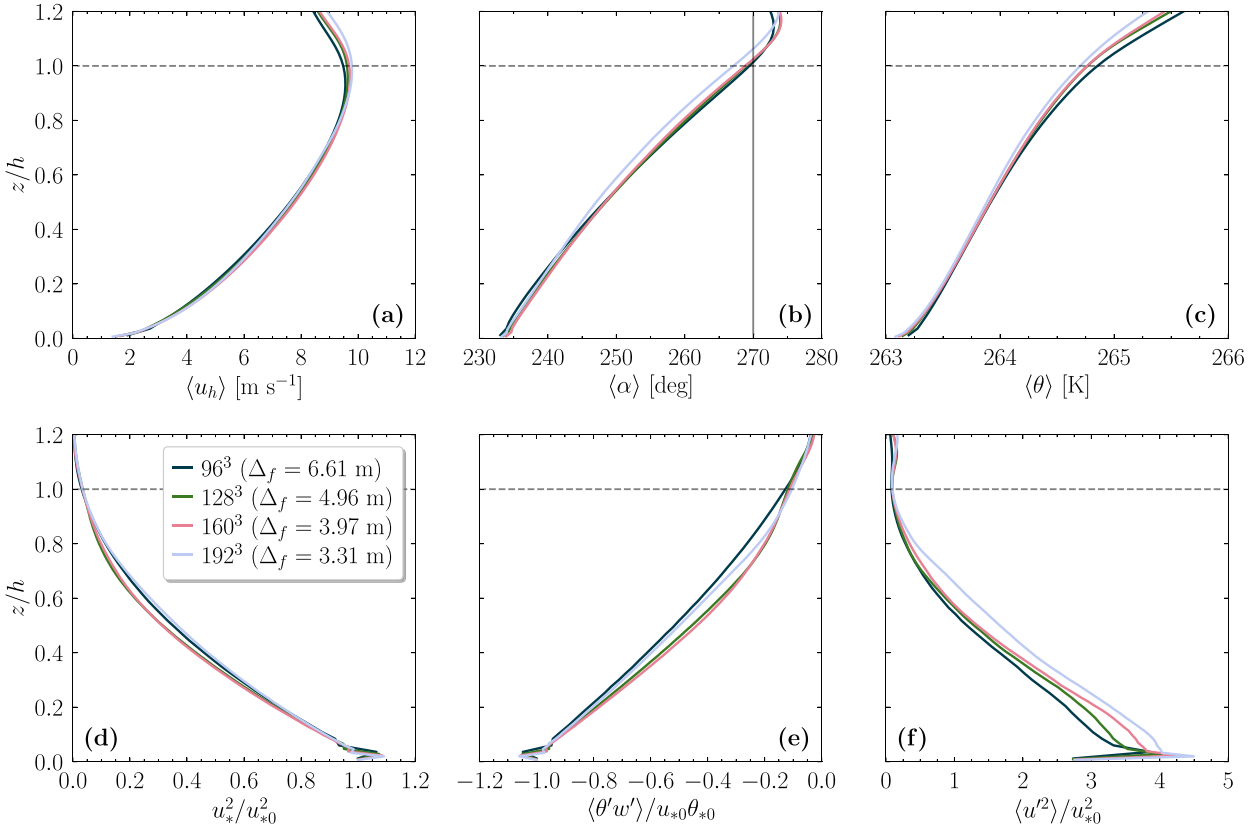

FIG. A1. Grid sensitivity for case A run at four different resolutions. Parameters are averaged in the xy plane over the last physical hour of simulation. (a) Wind speed, (b) wind direction, (c) potential temperature, (d) normalized momentum flux, (e) normalized heat flux, and (f) normalized streamwise velocity variance.

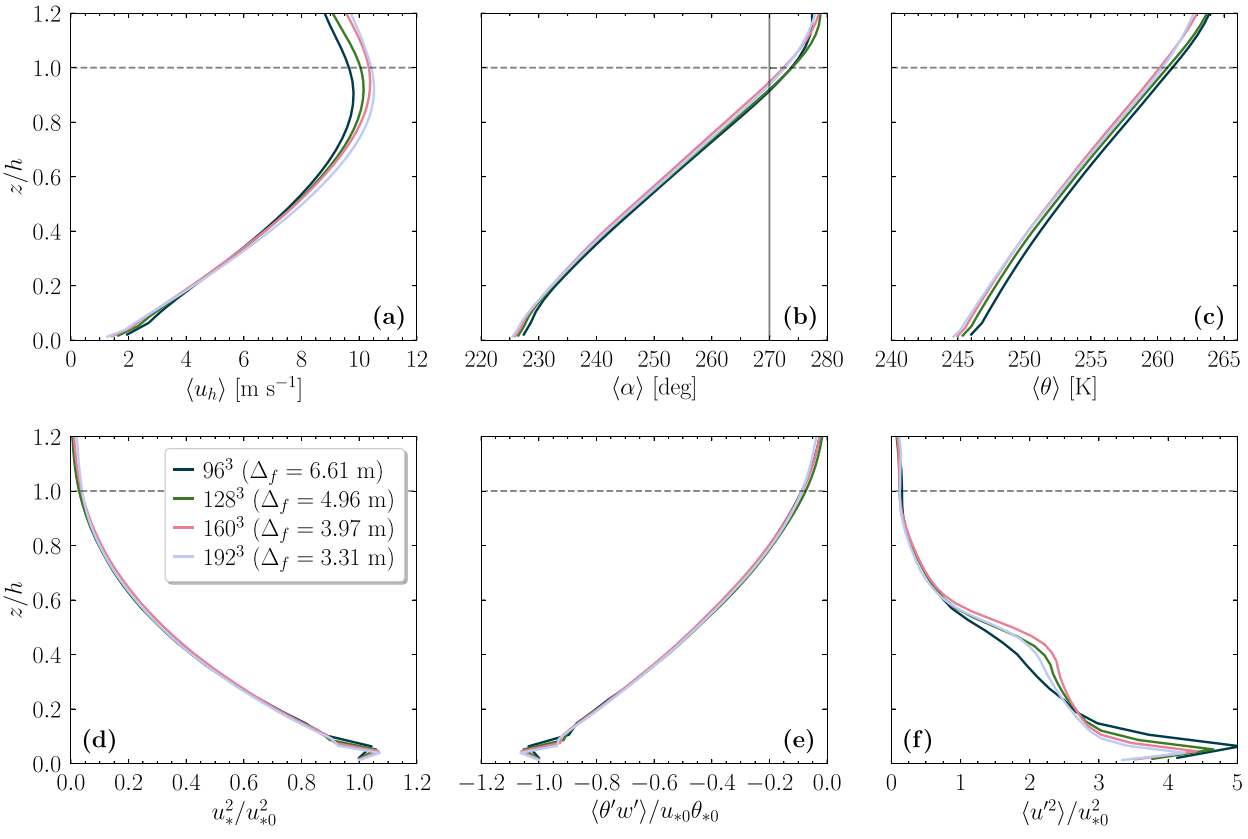

FIG. A2. As in Fig. A1, but for case F.

random errors in first-order quantities, especially close to the surface. Whenever possible, it would be advantageous to couple UAS operations with other ground-based sensors such as instrumented masts and remote sensors to better constrain the random errors for $z/h < 0.1$. Trade-offs between acceptable random errors and UAS ascent rates may also be necessary with considerations for UAS battery life.

It is important to recall that the random errors considered here are independent from errors arising due to instrument biases, imprecision, dynamic response, etc., but it is not clear how these error sources compound quantitatively. Since results indicate that random errors can be on the same order of magnitude as the other sources mentioned, they should therefore receive careful considerations in the context of NWP, data assimilation, and other general investigations of the SBL. We additionally acknowledge that only a limited parameter space was considered in this study, which is due in part to computational expense. Future work would ideally include iterations over model configurations such as flow over complex terrain and heterogeneous surface conditions to broaden this parameter space.

Acknowledgments. Financial assistance for this study was provided by the Office of the Vice President for Research and Partnerships (OVPRP) and the Cooperative Institute for Severe and High-Impact Weather Research and Operations (CIWRO) at the University of Oklahoma. STS gratefully acknowledges support from the National Science Foundation Grant OPP-2034874.

Data availability statement. Simulation data from the LES cases are available upon request to the corresponding author.

APPENDIX

Grid Convergence Tests

To investigate the effects of model grid spacing on our LES results, here we present the results from a series of grid convergence tests. The cases presented in this study were simulated in an $800 \times 800 \times 400$ m^3 domain with a numerical grid consisting of 192^3 total points. This was decided upon after first simulating cases A and F at additional resolutions of 96^3, 128^3, 160^3, and 192^3 (see Table A1). The 128^3, 160^3, and 192^3 simulations were first run at a resolution of 96^3 for 6 physical hours before being interpolated to their final resolution and continued for another 4 physical hours. The 96^3 simulation was run for 10 total hours without interpolation.

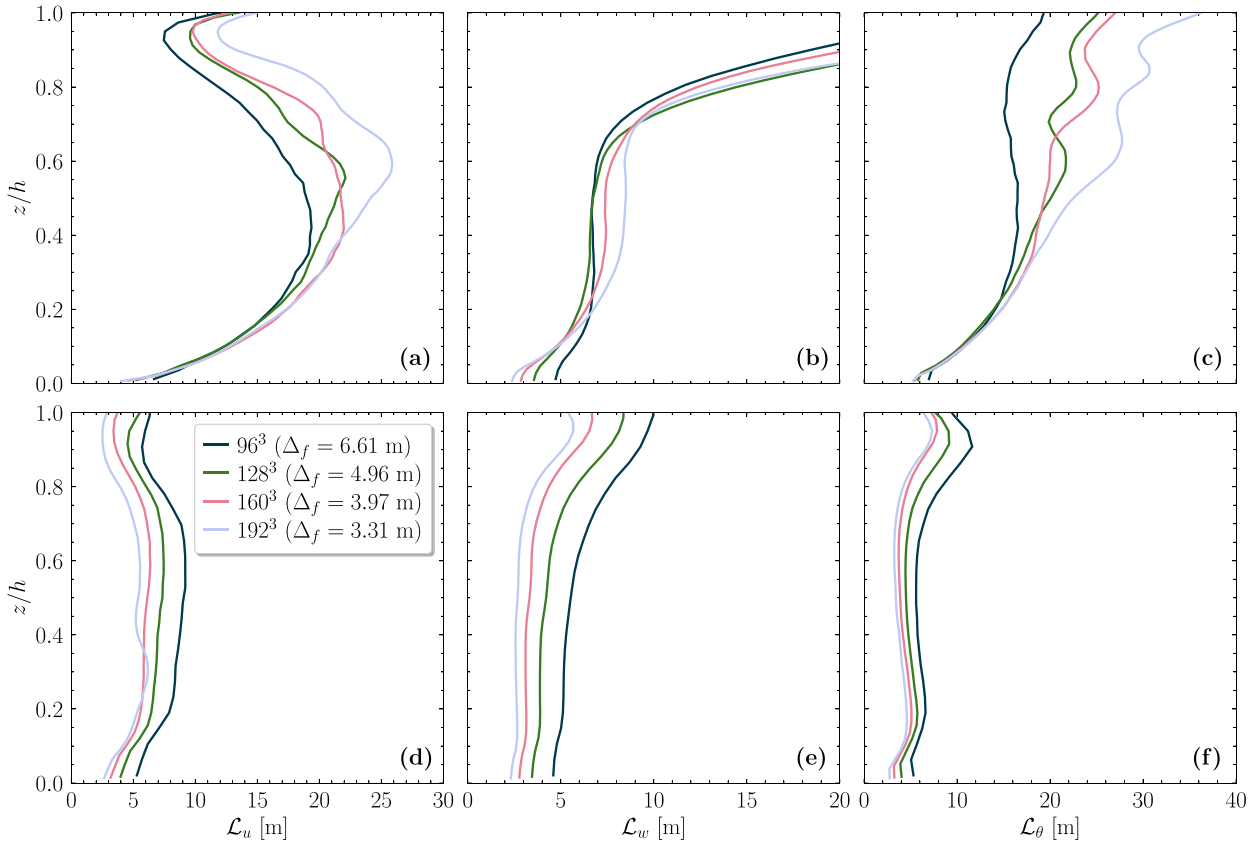

FIG. A3. Grid sensitivity for cases (top) A and (bottom) F. Plotted are integral length scales of (a),(d) streamwise velocity, (b),(e) vertical velocity, and (c),(f) potential temperature.

Mean profiles of relevant quantities are plotted in Fig. A1 for case A and Fig. A2 for case F, and simulation parameters are outlined in Table A1. The mean first-order profiles for case A (Figs. A1a–c) show clear convergence for resolutions of 128^3 and higher, whereas the second-order profiles (Figs. A1d–f) show stronger convergence at the 160^3 and higher resolutions. The 192^3 profile of normalized heat flux resides in between those from the 96^3 resolution and the 128^3 and 160^3 resolutions, which is most pronounced for $0.4 < z/h < 0.8$; however, this spread is ultimately not that large. The largest spread between resolutions for case A occurs in the normalized streamwise velocity variance profiles (Fig. A1f), with the largest difference occurring for $z/h < 0.3$. Of note for these profiles is that the dynamic Smagorinsky SGS model is only written for the deviatoric part of the SGS stress tensor, so the velocity variance components are determined as $\langle u'^2 \rangle = \langle \tilde{u}'\tilde{u}' \rangle$. Therefore, it is not entirely surprising that the convergence of the variance profiles will depend somewhat on model resolution as increasing energy can be resolved for increasing resolutions.

Similarly, in case F there is reasonable convergence among all profiles at resolutions of 160^3 and above. The maximum wind speed within the LLJ is slightly decreased at the 96^3 resolution, but this appears to converge on a similar value for increasing resolutions. The 96^3 potential temperature profile in Fig. A2c appears warmer than the others, possibly due to the limitations of the LES wall model at this relatively coarse resolution and low-level temperature gradients. The momentum and heat flux profiles demonstrate little to no dependence on resolution, which is a testament to the ability of the LASD SGS model to simulate the subgrid contributions of these terms (Bou-Zeid et al. 2005). Finally, the streamwise velocity variance profiles vary the most out of the parameters presented here, although the relatively small differences between the 160^3 and 192^3 resolutions imply a reasonable convergence.

Due to the relevance of the integral length scale to this study, in Fig. A3 are the resulting profiles of integral scales evaluated at each grid resolution for simulations A and F. For case A, in the lower half of the SBL all of the integral scales converge reasonably well at all resolutions. In the upper half of the SBL, there is some divergence in particular for $\mathcal{L}_u$ and $\mathcal{L}_\theta$, where it is observed that higher resolutions lead to larger integral length scales. This can perhaps be explained by the ability of the LES to resolve turbulence produced below the LLJ at finer and finer scales, which will lead to an enhancement in coherence. In case F it is notable that the integral scales grow slowly with increasing resolution for all parameters at all heights, and especially for $\mathcal{L}_w$ (Fig. A3e) which follows fairly closely with the LES filter width for each resolution considered. This is evidence that the LES filter extends toward the peak in resolved spectral

energy density, and the SGS model is heavily relied upon to model vertical transport at high stabilities. It therefore makes sense that the integral scales for case F tend to depend on LES grid resolution, as a finer grid will be able to explicitly resolve additional energy in the flow.

Overall, it is apparent that the 192^3 simulations provide a sufficient level of resolution for this study of random errors within the SBL. Although studies simulating the SBL with LES have been conducted at resolutions on the order of 1024^3 (e.g., Sullivan et al. 2016; Maronga and Li 2021), this type of model configuration is unobtainable with our current computational resources. Moreover, recent literature still reports a sensitivity to grid spacing even down to a spacing of 0.39 m wherein SBL heights continually decrease without a proper convergence (Sullivan et al. 2016; Maronga et al. 2020; Dai et al. 2021; Maronga and Li 2021). Although Maronga and Li (2021) recently recommend simulating closer to 40 physical hours instead of 10 as in studies based off the GABLS project (Beare et al. 2006; Huang and Bou-Zeid 2013), this is also computationally prohibitive. Regardless, for our study we believe the 192^3 resolution with $\Delta_f = 3.31$ m, when coupled with the LASD SGS model, is sufficient.

REFERENCES

Alaoui-Sosse, S., P. Durand, P. Medina, P. Pastor, M. Gavart, and S. Pizziol, 2022: BOREAL—A fixed-wing unmanned aerial system for the measurement of wind and turbulence in the atmospheric boundary layer. *J. Atmos. Oceanic Technol.*, **39**, 387–402, https://doi.org/10.1175/JTECH-D-21-0126.1.

Albertson, J. D., and M. B. Parlange, 1999: Surface length scales and shear stress: Implications for land-atmosphere interaction over complex terrain. *Water Resour. Res.*, **35**, 2121–2132, https://doi.org/10.1029/1999WR900094.

Aoyama, Y., and J. Nakano, 1999: RS/6000 SP: Practical MPI programming. IBM Redbooks Tech. Rep. SG24-5380-00, 238 pp., https://www.cs.kent.ac.uk/people/staff/trh/MPI/mpi_ibm.pdf.

Balsley, B. B., D. A. Lawrence, D. C. Fritts, L. Wang, K. Wan, and J. Werne, 2018: Fine structure, instabilities, and turbulence in the lower atmosphere: High-resolution in situ slant-path measurements with the DataHawk UAV and comparisons with numerical modeling. *J. Atmos. Oceanic Technol.*, **35**, 619–642, https://doi.org/10.1175/JTECH-D-16-0037.1.

Barbieri, L., and Coauthors, 2019: Intercomparison of small unmanned aircraft system (sUAS) measurements for atmospheric science during the LAPSE-RATE campaign. *Sensors*, **19**, 2179, https://doi.org/10.3390/s19092179.

Basu, S., A. A. M. Holtslag, B. J. H. Van De Wiel, A. F. Moene, and G.-J. Steeneveld, 2008: An inconvenient "truth" about using sensible heat flux as a surface boundary condition in models under stably stratified regimes. *Acta Geophys.*, **56**, 88–99, https://doi.org/10.2478/s11600-007-0038-y.

Beare, R. J., and Coauthors, 2006: An intercomparison of large-eddy simulations of the stable boundary layer. *Bound.-Layer Meteor.*, **118**, 247–272, https://doi.org/10.1007/s10546-004-2820-6.

Bell, T. M., B. R. Greene, P. M. Klein, M. Carney, and P. B. Chilson, 2020: Confronting the boundary layer data gap: Evaluating new and existing methodologies of probing the lower atmosphere. *Atmos. Meas. Tech.*, **13**, 3855–3872, https://doi.org/10.5194/amt-13-3855-2020.

Bevington, P. R., and D. K. Robinson, 1969: *Data Reduction and Error Analysis for the Physical Sciences*. McGraw-Hill, 150–153.

Bonin, T. A., P. M. Klein, and P. B. Chilson, 2020: Contrasting characteristics and evolution of southerly low-level jets during different boundary-layer regimes. *Bound.-Layer Meteor.*, **174**, 179–202, https://doi.org/10.1007/s10546-019-00481-0.

Bou-Zeid, E., C. Meneveau, and M. Parlange, 2005: A scale-dependent Lagrangian dynamic model for large eddy simulation of complex turbulent flows. *Phys. Fluids*, **17**, 025105, https://doi.org/10.1063/1.1839152.

Chilson, P. B., and Coauthors, 2019: Moving towards a network of autonomous UAS atmospheric profiling stations for observations in the Earth's lower atmosphere: The 3D mesonet concept. *Sensors*, **19**, 2720, https://doi.org/10.3390/s19122720.

Chinita, M. J., G. Matheou, and P. M. A. Miranda, 2022a: Large-eddy simulation of very stable boundary layers. Part I: Modeling methodology. *Quart. J. Roy. Meteor. Soc.*, **148**, 1805–1823, https://doi.org/10.1002/qj.4279.

——, ——, and ——, 2022b: Large-eddy simulation of very stable boundary layers. Part II: Length scales and anisotropy in stratified atmospheric turbulence. *Quart. J. Roy. Meteor. Soc.*, **148**, 1824–1839, https://doi.org/10.1002/qj.4280.

Dai, Y., S. Basu, B. Maronga, and S. R. de Roode, 2021: Addressing the grid-size sensitivity issue in large-eddy simulations of stable boundary layers. *Bound.-Layer Meteor.*, **178**, 63–89, https://doi.org/10.1007/s10546-020-00558-1.

de Boer, G., and Coauthors, 2020a: Development of community, capabilities, and understanding through unmanned aircraft-based atmospheric research: The LAPSE-RATE campaign. *Bull. Amer. Meteor. Soc.*, **101**, E684–E699, https://doi.org/10.1175/BAMS-D-19-0050.1.

——, and Coauthors, 2020b: Data generated during the 2018 LAPSE-RATE campaign: An introduction and overview. *Earth Syst. Sci. Data*, **12**, 3357–3366, https://doi.org/10.5194/essd-12-3357-2020.

——, and Coauthors, 2022: Measurements from the University of Colorado RAAVEN uncrewed aircraft system during ATOMIC. *Earth Syst. Sci. Data*, **14**, 19–31, https://doi.org/10.5194/essd-14-19-2022.

Dias, N. L., M. Chamecki, A. Kan, and C. M. P. Okawa, 2004: A study of spectra, structure and correlation functions and their implications for the stationarity of surface-layer turbulence. *Bound.-Layer Meteor.*, **110**, 165–189, https://doi.org/10.1023/A:1026067224894.

——, B. L. Crivellaro, and M. Chamecki, 2018: The Hurst phenomenon in error estimates related to atmospheric turbulence. *Bound.-Layer Meteor.*, **168**, 387–416, https://doi.org/10.1007/s10546-018-0353-7.

Finkelstein, P. L., and P. F. Sims, 2001: Sampling error in eddy correlation flux measurements. *J. Geophys. Res.*, **106**, 3503–3509, https://doi.org/10.1029/2000JD900731.

Flagg, D. D., and Coauthors, 2018: On the impact of unmanned aerial system observations on numerical weather prediction in the coastal zone. *Mon. Wea. Rev.*, **146**, 599–622, https://doi.org/10.1175/MWR-D-17-0028.1.

Fritz, A. M., K. Lapo, A. Freundorfer, T. Linhardt, and C. K. Thomas, 2021: Revealing the morning transition in the mountain boundary layer using fiber-optic distributed temperature sensing. *Geophys. Res. Lett.*, **48**, e2020GL092238, https://doi.org/10.1029/2020GL092238.

Gibbs, J. A., E. Fedorovich, and A. Shapiro, 2015: Revisiting surface heat-flux and temperature boundary conditions in models of

stably stratified boundary-layer flows. *Bound.-Layer Meteor.*, **154**, 171–187, https://doi.org/10.1007/s10546-014-9970-y.

González-Rocha, J., C. A. Woolsey, C. Sultan, and S. F. J. De Wekker, 2019: Sensing wind from quadrotor motion. *J. Guid. Control Dyn.*, **42**, 836–852, https://doi.org/10.2514/1.G003542.

——, S. F. J. De Wekker, S. D. Ross, and C. A. Woolsey, 2020: Wind profiling in the lower atmosphere from wind-induced perturbations to multirotor UAS. *Sensors*, **20**, 1341, https://doi.org/10.3390/s20051341.

Greene, B. R., A. R. Segales, S. Waugh, S. Duthoit, and P. B. Chilson, 2018: Considerations for temperature sensor placement on rotary-wing unmanned aircraft systems. *Atmos. Meas. Tech.*, **11**, 5519–5530, https://doi.org/10.5194/amt-11-5519-2018.

——, ——, T. M. Bell, E. A. Pillar-Little, and P. B. Chilson, 2019: Environmental and sensor integration influences on temperature measurements by rotary-wing unmanned aircraft systems. *Sensors*, **19**, 1470, https://doi.org/10.3390/s19061470.

——, S. T. Kral, P. B. Chilson, and J. Reuder, 2022: Gradient-based turbulence estimates from multicopter profiles in the Arctic stable boundary layer. *Bound.-Layer Meteor.*, **183**, 321–353, https://doi.org/10.1007/s10546-022-00693-x.

Higgins, C. W., M. G. Wing, J. Kelley, C. Sayde, J. Burnett, and H. A. Holmes, 2018: A high resolution measurement of the morning ABL transition using distributed temperature sensing and an unmanned aircraft system. *Environ. Fluid Mech.*, **18**, 683–693, https://doi.org/10.1007/s10652-017-9569-1.

Holtslag, A. M., and Coauthors, 2013: Stable atmospheric boundary layers and diurnal cycles: Challenges for weather and climate models. *Bull. Amer. Meteor. Soc.*, **94**, 1691–1706, https://doi.org/10.1175/BAMS-D-11-00187.1.

Houston, A. L., and J. M. Keeler, 2018: The impact of sensor response and airspeed on the representation of the convective boundary layer and airmass boundaries by small unmanned aircraft systems. *J. Atmos. Oceanic Technol.*, **35**, 1687–1699, https://doi.org/10.1175/JTECH-D-18-0019.1.

——, and ——, 2020: Sounding characteristics that yield significant convective inhibition errors due to ascent rate and sensor response of in situ profiling systems. *J. Atmos. Oceanic Technol.*, **37**, 1163–1172, https://doi.org/10.1175/JTECH-D-19-0191.1.

——, L. M. PytlikZillig, and J. C. Walther, 2021: National Weather Service data needs for short-term forecasts and the role of unmanned aircraft in filling the gap: Results from a nationwide survey. *Bull. Amer. Meteor. Soc.*, **102**, E2106–E2120, https://doi.org/10.1175/BAMS-D-20-0183.1.

Huang, J., and E. Bou-Zeid, 2013: Turbulence and vertical fluxes in the stable atmospheric boundary layer. Part I: A large-eddy simulation study. *J. Atmos. Sci.*, **70**, 1513–1527, https://doi.org/10.1175/JAS-D-12-0167.1.

——, ——, and J.-C. Golaz, 2013: Turbulence and vertical fluxes in the stable atmospheric boundary layer. Part II: A novel mixing-length model. *J. Atmos. Sci.*, **70**, 1528–1542, https://doi.org/10.1175/JAS-D-12-0168.1.

Hurst, H. E., 1951: Long-term storage capacity of reservoirs. *Trans. Amer. Soc. Civ. Eng.*, **116**, 770–799, https://doi.org/10.1061/TACEAT.0006518.

Islam, A., A. Shankar, A. Houston, and C. Detweiler, 2021: University of Nebraska unmanned aerial system (UAS) profiling during the LAPSE-RATE field campaign. *Earth Syst. Sci. Data*, **13**, 2457–2470, https://doi.org/10.5194/essd-13-2457-2021.

Jensen, A. A., and Coauthors, 2021: Assimilation of a coordinated fleet of uncrewed aircraft system observations in complex terrain: EnKF system design and preliminary assessment. *Mon. Wea. Rev.*, **149**, 1459–1480, https://doi.org/10.1175/MWR-D-20-0359.1.

——, and Coauthors, 2022: Assimilation of a coordinated fleet of uncrewed aircraft system observations in complex terrain: Observing system experiments. *Mon. Wea. Rev.*, **150**, 2737–2763, https://doi.org/10.1175/MWR-D-22-0090.1.

Joyce, K. E., K. Anderson, and R. E. Bartolo, 2021: Of course we fly unmanned—We're women! *Drones*, **5**, 21, https://doi.org/10.3390/drones5010021.

Kaimal, J. C., and J. J. Finnigan, 1994: *Atmospheric Boundary Layer Flows: Their Structure and Measurement*. Oxford University Press, 304 pp.

Kosović, B., and J. A. Curry, 2000: A large eddy simulation study of a quasi-steady, stably stratified atmospheric boundary layer. *J. Atmos. Sci.*, **57**, 1052–1068, https://doi.org/10.1175/1520-0469(2000)057<1052:ALESSO>2.0.CO;2.

Kral, S. T., and Coauthors, 2018: Innovative Strategies for Observations in the Arctic Atmospheric Boundary Layer (ISOBAR)—The Hailuoto 2017 campaign. *Atmosphere*, **9**, 268, https://doi.org/10.3390/atmos9070268.

——, and Coauthors, 2021: The Innovative Strategies for Observations in the Arctic Atmospheric Boundary Layer project (ISOBAR): Unique finescale observations under stable and very stable conditions. *Bull. Amer. Meteor. Soc.*, **102**, E218–E243, https://doi.org/10.1175/BAMS-D-19-0212.1.

Krautwurst, S., and Coauthors, 2021: Quantification of CH_4 coal mining emissions in Upper Silesia by passive airborne remote sensing observations with the Methane Airborne Mapper (MAMAP) instrument during the CO_2 and Methane (CoMet) campaign. *Atmos. Chem. Phys.*, **21**, 17 345–17 371, https://doi.org/10.5194/acp-21-17345-2021.

Kumar, V., J. Kleissl, C. Meneveau, and M. B. Parlange, 2006: Large-eddy simulation of a diurnal cycle of the atmospheric boundary layer: Atmospheric stability and scaling issues. *Water Resour. Res.*, **42**, W06D09, https://doi.org/10.1029/2005WR004651.

Lapo, K., A. Freundorfer, A. Fritz, J. Schneider, J. Olesch, W. Babel, and C. K. Thomas, 2022: The Large eddy Observatory, Voitsumra Experiment 2019 (LOVE19) with high-resolution, spatially distributed observations of air temperature, wind speed, and wind direction from fiber-optic distributed sensing, towers, and ground-based remote sensing. *Earth Syst. Sci. Data*, **14**, 885–906, https://doi.org/10.5194/essd-14-885-2022.

Lappin, F. M., T. M. Bell, E. A. Pillar-Little, and P. B. Chilson, 2022: Low-level buoyancy as a tool to understand boundary layer transitions. *Atmos. Meas. Tech.*, **15**, 1185–1200, https://doi.org/10.5194/amt-15-1185-2022.

Launiainen, J., and T. Vihma, 1990: Derivation of turbulent surface fluxes—An iterative flux-profile method allowing arbitrary observing heights. *Environ. Software*, **5**, 113–124, https://doi.org/10.1016/0266-9838(90)90021-W.

Lenschow, D. H., J. Mann, and L. Kristensen, 1994: How long is long enough when measuring fluxes and other turbulence statistics? *J. Atmos. Oceanic Technol.*, **11**, 661–673, https://doi.org/10.1175/1520-0426(1994)011<0661:HLILEW>2.0.CO;2.

Lumley, J., and H. Panofsky, 1964: *The Structure of Atmospheric Turbulence*. Interscience Publishers, 239 pp.

Mann, J., and D. H. Lenschow, 1994: Errors in airborne flux measurements. *J. Geophys. Res.*, **99**, 14 519–14 526, https://doi.org/10.1029/94JD00737.

Maronga, B., and D. Li, 2021: An investigation of the grid sensitivity in large-eddy simulations of the stable boundary layer.

Bound.-Layer Meteor., **182**, 251–273, https://doi.org/10.1007/s10546-021-00656-8.

——, C. Knigge, and S. Raasch, 2020: An improved surface boundary condition for large-eddy simulations based on Monin–Obukhov similarity theory: Evaluation and consequences for grid convergence in neutral and stable conditions. *Bound.-Layer Meteor.*, **174**, 297–325, https://doi.org/10.1007/s10546-019-00485-w.

Monin, A. S., and A. M. Obukhov, 1954: Basic laws of turbulent mixing in the atmosphere near the ground. *Tr. Geofiz. Inst., Akad. Nauk SSSR*, **24**, 163–187.

Moore, A., 2018: Observing system simulation experiment studies on the use of small UAV for boundary-layer sampling. M.S. thesis, Dept. of Meteorology, University of Oklahoma, 147 pp.

Nieuwstadt, F. T. M., P. J. Mason, C.-H. Moeng, and U. Schumann, 1993: Large-eddy simulation of the convective boundary layer: A comparison of four computer codes. *Turbulent Shear Flows 8*, F. Durst et al., Eds., Springer, 343–367, https://doi.org/10.1007/978-3-642-77674-8_24.

O'Connell, P. E., D. Koutsoyiannis, H. F. Lins, Y. Markonis, A. Montanari, and T. Cohn, 2016: The scientific legacy of Harold Edwin Hurst (1880–1978). *Hydrol. Sci. J.*, **61**, 1571–1590, https://doi.org/10.1080/02626667.2015.1125998.

Peltola, O., K. Lapo, I. Martinkauppi, E. O'Connor, C. K. Thomas, and T. Vesala, 2021: Suitability of fibre-optic distributed temperature sensing for revealing mixing processes and higher-order moments at the forest–air interface. *Atmos. Meas. Tech.*, **14**, 2409–2427, https://doi.org/10.5194/amt-14-2409-2021.

Pillar-Little, E. A., and Coauthors, 2021: Observations of the thermodynamic and kinematic state of the atmospheric boundary layer over the San Luis Valley, CO, using the CopterSonde 2 remotely piloted aircraft system in support of the LAPSE-RATE field campaign. *Earth Syst. Sci. Data*, **13**, 269–280, https://doi.org/10.5194/essd-13-269-2021.

Pinto, J. O., and Coauthors, 2021: The status and future of small uncrewed aircraft systems (UAS) in operational meteorology. *Bull. Amer. Meteor. Soc.*, **102**, E2121–E2136, https://doi.org/10.1175/BAMS-D-20-0138.1.

Rautenberg, A., and Coauthors, 2019: The Multi-Purpose Airborne Sensor Carrier MASC-3 for wind and turbulence measurements in the atmospheric boundary layer. *Sensors*, **19**, 2292, https://doi.org/10.3390/s19102292.

Sagaut, P., 2006: *Large Eddy Simulation for Incompressible Flows: An Introduction*. 3rd ed. Springer, 556 pp.

Salesky, S. T., and M. Chamecki, 2012: Random errors in turbulence measurements in the atmospheric surface layer: Implications for Monin–Obukhov similarity theory. *J. Atmos. Sci.*, **69**, 3700–3714, https://doi.org/10.1175/JAS-D-12-096.1.

——, and W. Anderson, 2018: Buoyancy effects on large-scale motions in convective atmospheric boundary layers: Implications for modulation of near-wall processes. *J. Fluid Mech.*, **856**, 135–168, https://doi.org/10.1017/jfm.2018.711.

——, M. Chamecki, and N. L. Dias, 2012: Estimating the random error in eddy-covariance based fluxes and other turbulence statistics: The filtering method. *Bound.-Layer Meteor.*, **144**, 113–135, https://doi.org/10.1007/s10546-012-9710-0.

Sandu, I., A. Beljaars, P. Bechtold, T. Mauritsen, and G. Balsamo, 2013: Why is it so difficult to represent stably stratified conditions in numerical weather prediction (NWP) models? *J. Adv. Model. Earth Syst.*, **5**, 117–133, https://doi.org/10.1002/jame.20013.

Schuyler, T. J., and M. I. Guzman, 2017: Unmanned aerial systems for monitoring trace tropospheric gases. *Atmosphere*, **8**, 206, https://doi.org/10.3390/atmos8100206.

Segales, A. R., B. R. Greene, T. M. Bell, W. Doyle, J. J. Martin, E. A. Pillar-Little, and P. B. Chilson, 2020: The CopterSonde: An insight into the development of a smart unmanned aircraft system for atmospheric boundary layer research. *Atmos. Meas. Tech.*, **13**, 2833–2848, https://doi.org/10.5194/amt-13-2833-2020.

——, P. B. Chilson, and J. L. Salazar-Cerreño, 2022: Considerations for improving data quality of thermo-hygrometer sensors on board unmanned aerial systems for planetary boundary layer research. *Atmos. Meas. Tech.*, **15**, 2607–2621, https://doi.org/10.5194/amt-2021-316.

Shenoy, V., 2021: Observing system simulation experiments using small unmanned aerial vehicles in various configurations to improve high-resolution forecasts of convection. M.S. thesis, Dept. of Meteorology, University of Oklahoma, 177 pp.

Smith, E. N., J. G. Gebauer, P. M. Klein, E. Fedorovich, and J. A. Gibbs, 2019: The Great Plains low-level jet during PECAN: Observed and simulated characteristics. *Mon. Wea. Rev.*, **147**, 1845–1869, https://doi.org/10.1175/MWR-D-18-0293.1.

——, and Coauthors, 2021: Evaluation and applications of multi-instrument boundary-layer thermodynamic retrievals. *Bound.-Layer Meteor.*, **181**, 95–123, https://doi.org/10.1007/s10546-021-00640-2.

Sorbjan, Z., 2017: Assessment of gradient-based similarity functions in the stable boundary layer derived from a large-eddy simulation. *Bound.-Layer Meteor.*, **163**, 375–392, https://doi.org/10.1007/s10546-017-0234-5.

Sreenivasan, K. R., A. J. Chambers, and R. A. Antonia, 1978: Accuracy of moments of velocity and scalar fluctuations in the atmospheric surface layer. *Bound.-Layer Meteor.*, **14**, 341–359, https://doi.org/10.1007/BF00121044.

Steeneveld, G. J., T. Mauritsen, E. I. F. de Bruijn, J. Vilà-Guerau de Arellano, G. Svensson, and A. M. Holtslag, 2008: Evaluation of limited-area models for the representation of the diurnal cycle and contrasting nights in CASES-99. *J. Appl. Meteor. Climatol.*, **47**, 869–887, https://doi.org/10.1175/2007JAMC1702.1.

Stoll, R., J. A. Gibbs, S. T. Salesky, W. Anderson, and M. Calaf, 2020: Large-eddy simulation of the atmospheric boundary layer. *Bound.-Layer Meteor.*, **177**, 541–581, https://doi.org/10.1007/s10546-020-00556-3.

Sullivan, P. P., T. W. Horst, D. H. Lenschow, C.-H. Moeng, and J. C. Weil, 2003: Structure of subfilter-scale fluxes in the atmospheric surface layer with application to large-eddy simulation modelling. *J. Fluid Mech.*, **482**, 101–139, https://doi.org/10.1017/S0022112003004099.

——, J. C. Weil, E. G. Patton, H. J. J. Jonker, and D. V. Mironov, 2016: Turbulent winds and temperature fronts in large-eddy simulations of the stable atmospheric boundary layer. *J. Atmos. Sci.*, **73**, 1815–1840, https://doi.org/10.1175/JAS-D-15-0339.1.

Theunissen, R., A. Di Sante, M. L. Riethmuller, and R. A. Van den Braembussche, 2008: Confidence estimation using dependent circular block bootstrapping: Application to the statistical analysis of PIV measurements. *Exp. Fluids*, **44**, 591–596, https://doi.org/10.1007/s00348-007-0418-8.

Tritton, D. J., 1988: *Physical Fluid Dynamics*. 2nd ed. Oxford University Press, 519 pp.

van den Heever, S. C., and Coauthors, 2021: The Colorado State University Convective Cloud Outflows and Updrafts Experiment (C3LOUD-Ex). *Bull. Amer. Meteor. Soc.*, **102**, E1283–E1305, https://doi.org/10.1175/BAMS-D-19-0013.1.

van der Linden, S. J. A., and Coauthors, 2019: Large-eddy simulations of the steady wintertime Antarctic boundary layer. *Bound.-Layer Meteor.*, **173**, 165–192, https://doi.org/10.1007/s10546-019-00461-4.

van de Wiel, B. J. H., A. F. Moene, W. H. De Ronde, and H. J. J. Jonker, 2008: Local similarity in the stable boundary layer and mixing-length approaches: Consistency of concepts. *Bound.-Layer Meteor.*, **128**, 103–116, https://doi.org/10.1007/s10546-008-9277-y.

Wyngaard, J. C., and O. R., Coté, 1971: The budgets of turbulent kinetic energy and temperature variance in the atmospheric surface layer. *J. Atmos. Sci.*, **28**, 190–201, https://doi.org/10.1175/1520-0469(1971)028<0190:TBOTKE>2.0.CO;2.

Wildmann, N., M. Hofsäß, F. Weimer, A. Joos, and J. Bange, 2014: MASC—A small remotely piloted aircraft (RPA) for wind energy research. *Adv. Sci. Res.*, **11**, 55–61, https://doi.org/10.5194/asr-11-55-2014.

Zilitinkevich, S. S., 1989: Velocity profiles, the resistance law and the dissipation rate of mean flow kinetic energy in a neutrally and stably stratified planetary boundary layer. *Bound.-Layer Meteor.*, **46**, 367–387, https://doi.org/10.1007/BF00172242.